The Astrophysical Journal, 706:535–552, 2009 November 20 doi:10.1088/0004-637X/706/1/535


# HEAVILY OBSCURED AGN IN STAR-FORMING GALAXIES AT $z \simeq 2$*

E. Treister[1,10], Carolin N. Cardamone[2,3], Kevin Schawinski[2,3,10], C. Megan Urry[2,3,4], Eric Gawiser[5], Shanil Virani[2,3], Paulina Lira[6], Jeyhan Kartaltepe[1], Maaike Damen[7], Edward N. Taylor[7], Emeric Le Floc'h[1], Stephen Justham[8], and Anton M. Koekemoer[9]

[1] Institute for Astronomy, 2680 Woodlawn Drive, University of Hawaii, Honolulu, HI 96822, USA; treister@ifa.hawaii.edu
[2] Department of Astronomy, Yale University, P.O. Box 208101, New Haven, CT 06520, USA
[3] Yale Center for Astronomy and Astrophysics, P.O. Box 208121, New Haven, CT 06520, USA
[4] Department of Physics, Yale University, P.O. Box 208121, New Haven, CT 06520, USA
[5] Department of Physics and Astronomy, Rutgers University, 136 Frelinghuysen Road, Piscataway, NJ 08854-8019, USA
[6] Departamento de Astronomía, Universidad de Chile, Casilla 36-D, Santiago, Chile
[7] Sterrewacht Leiden, Leiden University, NL-2300 RA Leiden, Netherlands
[8] Kavli Institute for Astronomy and Astrophysics, Peking University, Beijing, China
[9] Space Telescope Science Institute, 3700 San Martin Drive, Baltimore, MD 21218, USA
*Received 2009 June 26; accepted 2009 October 9; published 2009 November 2*

## ABSTRACT

We study the properties of a sample of 211 heavily obscured active galactic nucleus (AGN) candidates in the extended Chandra Deep Field-South selecting objects with $f_{24\,\mu m}/f_R > 1000$ and $R - K > 4.5$. Of these, 18 were detected in X-rays and found to be obscured AGNs with neutral hydrogen column densities of $\sim 10^{23}$ cm$^{-2}$. In the X-ray-undetected sample, the following evidence suggests a large fraction of heavily obscured (Compton-thick) AGN: (1) The stacked X-ray signal of the sample is strong, with an observed ratio of soft to hard X-ray counts consistent with a population of ∼90% heavily obscured AGNs combined with 10% star-forming galaxies. (2) The X-ray-to-mid-IR ratios for these sources are significantly larger than that of star-forming galaxies and ∼2 orders of magnitude smaller than for the general AGN population, suggesting column densities of $N_H \gtrsim 5 \times 10^{24}$ cm$^{-2}$. (3) The *Spitzer* near- and mid-IR colors of these sources are consistent with those of the X-ray-detected samples if the effects of dust self-absorption are considered. Spectral fitting to the rest-frame UV/optical light (dominated by the host galaxy) returns stellar masses of $\sim 10^{11} M_\odot$ and $\langle E(B-V) \rangle = 0.5$, and reveals evidence for a significant young stellar population, indicating that these sources are experiencing considerable star formation. This sample of heavily obscured AGN candidates implies a space density at $z \sim 2$ of $\sim 10^{-5}$ Mpc$^{-3}$, finding a strong evolution in the number of $L_X > 10^{44}$ erg s$^{-1}$ sources from $z = 1.5$ to 2.5, possibly consistent with a short-lived heavily obscured phase before an unobscured quasar is visible.

*Key words:* galaxies: active – galaxies: Seyfert – X-rays: diffuse background – X-rays: galaxies

*Online-only material:* color figures

## 1. INTRODUCTION

Understanding the processes of galaxy formation and evolution is one of the outstanding problems of modern astronomy. It is now clear that the growth and feeding of the central black hole of an active galactic nucleus (AGN) and the formation of its host galaxy must be intimately connected, as evidenced by the striking correlations between the properties of supermassive black holes and the stellar systems in which they reside (Magorrian et al. 1998; Gebhardt et al. 2000; Ferrarese et al. 2001). Furthermore, it is now strongly suspected that AGN activity is critical in the regulation of star formation in the host galaxy either by removing all the gas (e.g., Hopkins et al. 2006; Menci et al. 2006) by heating it (e.g. Croton et al. 2006) or both (Schawinski et al. 2006). However, an observational link between AGN activity and quenching of star formation has not yet been established (e.g., Schawinski et al. 2009). To understand how the AGN and galaxy formation processes are connected requires a detailed census of the AGN population as well as detailed study of individual objects.

The visibility and detectability of an AGN are determined by the interplay among black hole mass, accretion rate, gas distribution, dust geometry, and the amount of star formation in the host galaxy. Thus, no single selection method provides a complete view of how galaxies and AGN co-evolve. Many surveys (e.g., Barger et al. 2001; Cowie et al. 2002; see Brandt & Hasinger 2005 for a review) have focused on X-ray selection because X-ray emission is a universal feature of AGN accretion. However, X-ray selection has limited sensitivity to heavily obscured and/or low accretion rate sources, even in the deepest surveys (Treister et al. 2004). In particular, examples of the most heavily obscured AGN, the so-called Compton-thick (CT) AGN, which have $\tau \sim 1$ for Compton scattering or $N_H \sim 10^{24}$ cm$^{-2}$, are mostly found in the local universe. Only a few of these sources have been identified at higher redshifts, although this is simply due to selection effects (Della Ceca et al. 2008b). In contrast, early AGN population synthesis models that can fit the X-ray background (XRB) spectral shape and intensity (Treister & Urry 2005; Gilli et al. 2007) require ∼20%–30% CT AGNs in order to explain the observed peak at ∼30 keV in the XRB radiation. Recently, Treister et al. (2009a) combined observations of local ($z < 0.05$) AGNs at very hard X-rays ($E > 20$ keV), using the *International Gamma-Ray Astrophysics Laboratory* (*INTEGRAL*) and *Swift* satellites, with XRB models and concluded that the CT AGN fraction is only ∼10% at these redshifts. They conclude that CT AGNs represent a similarly small fraction of the total XRB radiation and total

* Partly based on observations collected at the European Southern Observatory, Chile, under program 080.A-0612.
[10] Chandra/Einstein Fellow.

black hole growth. However, because only ∼2% of the XRB comes from CT AGNs at $z > 2$ and only a few sources are known at such high redshifts, this population still remains basically unconstrained, with up to an order of magnitude uncertainty in number density (Treister et al. 2009a).

Because the energy absorbed at optical to X-ray wavelengths is later re-emitted in the mid-IR, it is expected that AGNs, in particular the most obscured ones, should be very bright mid-IR sources (Treister et al. 2006 and references therein), easily detectable in observations with the *Spitzer* observatory. Sources having mid-IR excesses, relative to their rest-frame optical and UV emission, have been identified as potential CT AGN candidates at $z \sim 2$ (Daddi et al. 2007; Fiore et al. 2008; Georgantopoulos et al. 2008 and others). However, because of the strong connection between vigorous star formation and AGN activity in the most luminous infrared sources (Sanders et al. 1988), the relative contribution of these processes is still uncertain and remains controversial (e.g., Donley et al. 2008; Pope et al. 2008).

In order to detect CT AGNs up to high redshifts, deep multiwavelength coverage is critical. The extended Chandra Deep Field-South (ECDF-S) is one of the best fields to carry out this study. The rich multiwavelength data available in the ECDF-S include four ∼250 ks Chandra pointings covering an area of ∼0.3 deg$^2$, and deep *Spitzer* data in the IRAC bands from the *Spitzer* IRAC/MUSYC Public Legacy in ECDF-S (SIMPLE) survey and at 24 $\mu$m from the Far-Infrared Deep Extragalactic Legacy Survey (FIDEL). The 24 $\mu$m depth in this field is ∼35 $\mu$Jy, comparable to the deep Great Observatories Origins Deep Survey (GOODS) observations.

In this paper, we present a study of the properties of the CT AGN candidates in the ECDF-S selected from their 24 $\mu$m to optical flux ratio and rest-frame optical to UV colors. In Section 2, we describe the multiwavelength data used in this work, while our selection scheme is presented in Section 3. The properties of the sources individually detected in X-rays are discussed in Section 4, while the remaining sources are studied in Section 5. The near- and mid-IR colors, X-ray to mid-IR flux ratios and space density of our sources are presented in Section 6, and our conclusions are reported in Section 7. We assume a ΛCDM cosmology with $h_0 = 0.7$, $\Omega_m = 0.3$, and $\Omega_\Lambda = 0.7$, in agreement with the most recent cosmological observations (Spergel et al. 2007).

## 2. MULTIWAVELENGTH DATA

### 2.1. X-ray Data

The full ECDF-S was covered by Chandra as part of a Cycle 5 guest observer program (PI: N. Brandt). The total area covered is ∼0.3 deg$^2$ to a depth of ≃230 ks. Details about these observations, images, and catalogs were presented separately by Lehmer et al. (2005) and Virani et al. (2006). The work of Lehmer et al. (2005) reports the finding of 762 sources to flux limits of $1.1 \times 10^{-16}$ and $6.7 \times 10^{-16}$ erg cm$^{-2}$ s$^{-1}$ in the soft (0.5–2 keV) and hard (2–8 keV) bands. The catalog of Virani et al. (2006) includes 651 sources to similar flux limits, using a more conservative rejection of periods of higher background, thus reducing the number of spurious sources but excluding a few real sources as well. In this work, we use mainly the Virani et al. (2006) catalog. However, when performing stacking analysis, we further exclude sources individually detected in the Lehmer et al. (2005) catalog and/or in the deeper 1 and 2 Ms observations available in the central ≃0.1 deg$^2$, presented by Alexander et al. (2003) and Luo et al. (2008), respectively.

### 2.2. Mid-IR Data

The ECDF-S was observed extensively at near and mid-IR wavelengths by the *Spitzer Space Telescope*. The central $10' \times 16'$ region was covered using both the Infrared Array Camera (IRAC; Fazio et al. 2004) and the Multiband Imaging Photometer for *Spitzer* (MIPS; Rieke et al. 2004). These observations were performed as part of the GOODS survey and guaranteed time programs. More details about these observations were presented by Treister et al. (2006) and R. Chary et al. (2009, in preparation).

The extended $30' \times 30'$ region was observed by IRAC as part of the SIMPLE survey. The flux limits for the SIMPLE observations are 0.76, 0.4, 5.8, and 3.6 $\mu$Jy in the 3.6, 4.5 and 5.7, and 8 $\mu$m bands, respectively, or ∼3–5 times shallower than the GOODS observations. More details about the IRAC coverage of the ECDF-S were reported by Cardamone et al. (2008) and M. Damen et al. (2009, in preparation). When required, the conversion factors from flux density to Vega magnitudes provided by Fazio et al. (2004) were assumed. The ECDF-S was also observed at longer wavelengths in the FIDEL survey, which obtained data at 24, 70, and 160 $\mu$m. Because of the significant decrease in sensitivity at longer wavelengths, mainly due to source confusion, only the 24 $\mu$m data are considered in this work. Details about the data reduction and catalog creation were presented by Treister et al. (2009b). The approximate flux limit of the 24 $\mu$m data used here is ∼35 $\mu$Jy. For comparison, the flux limit of the GOODS 24 $\mu$m data is ∼12 $\mu$Jy (Daddi et al. 2007), while Fiore et al. (2008) studied only sources with $f_{24} > 40$ $\mu$Jy in the Chandra Deep Field South (CDF-S) proper. The work of Fiore et al. (2009) in the COSMOS field used only the shallow cycle 2 MIPS data to a flux limit of ∼550 $\mu$Jy.

### 2.3. Optical/Near-IR Data

The ECDF-S was observed at optical wavelengths using both ground-based and space telescopes. Deep images (to $V \sim 26.5$) in the *UBVRI* were obtained using the Wide Field Imager (WFI) on the 2.2 m telescope at La Silla. These data were made public by the ESO Deep Public Survey (Mignano et al. 2007), COMBO-17 (Wolf et al. 2004), and Garching-Bonn Deep Survey (GaBODS; Hildebrandt et al. 2006) teams. Imaging to $z' = 23.6$ AB, was performed using the MOSAIC-II camera mounted on the Blanco 4 m telescope at Cerro Tololo (Gawiser et al. 2006b). The *Hubble Space Telescope* observed the ECDF-S in the $V$ and $z'$ bands as part of the Galaxy Evolution from Morphology and SEDs (GEMS) survey (Rix et al. 2004). Deep near-IR coverage was obtained using the CTIO 4 m telescope with the Infrared Sideport Imager (ISPI), reaching a magnitude limit of ∼22 (AB) in the $JHK_s$ bands (Taylor et al. 2009), as part of the Multiwavelength Survey by Yale–Chile (MUSYC; Gawiser et al. 2006a; Treister et al. 2007).

In order to obtain high-quality photometric redshifts, the ECDF-S was imaged in 18 medium-band optical filters using the wide-field Suprime Camera on the Subaru telescope. These filters range from 4270 to 8560 Å and are optimized for photometric redshift determinations (Hayashino et al. 2000). The data reach an average depth of ∼26 magnitudes ($5\sigma$, AB), extending redshift determinations to sources much fainter than most spectroscopic redshift surveys. More details about these observations, data reduction and catalogs will be presented by C. Cardamone et al. (2009, in preparation) and in Section 2.5.

### 2.4. Spectroscopic Redshifts

Rich optical spectroscopic data exist in the ECDF-S. We took advantage of the ESO/GOODS-CDFS spectroscopy master catalogue[11] which compiles spectroscopic data from 11 different sources, mostly using 8–10 m class telescopes. In particular, many of the spectroscopic redshifts for the X-ray sources in the CDF-S proper were reported by Szokoly et al. (2004) using the VLT telescopes with the FORS1/FORS2 spectrographs. In addition, spectroscopic observations for 339 X-ray sources in the ECDF-S field using the VLT/VIMOS and Magellan/IMACS are reported by Treister et al. (2009b).

Given the very faint optical magnitudes of the ECDF-S X-ray sources, obtaining redshifts and identifications is a very hard, time-demanding task. In particular, optical spectroscopy is often out of reach, even for state-of-the-art 10 m-class telescopes. However, near-IR spectroscopy offers a higher chance of success, not only because these sources are significantly brighter at these wavelengths, but more importantly because, based on the experience with similar sources in other fields, they are found at redshifts $z = 1$–3, where the typical optical emission lines are shifted to the near-IR. For the brighter sources we used the Spectrograph for INtegral Field Observations in the Near Infrared (SINFONI; Eisenhauer et al. 2003; Bonnet et al. 2004) at the VLT, and the Multi-Object InfraRed Camera and Spectrograph (MOIRCS; Ichikawa et al. 2006; Suzuki et al. 2008) at the Subaru 8 m telescope. For the remaining sources in our sample, we have to rely on photometric redshifts, which are relatively accurate because of the deep Subaru medium-band photometry described below.

#### 2.4.1. SINFONI Data

A total of 16 hr were granted to observe four X-ray sources in the ECDF-S with $V-K > 7$ using the VLT/SINFONI Integral Field Unit (IFU) as part of program 080.A-0612. The observations were carried out in service mode by the Paranal staff in the 2007 October-2008 January period. We attempted to observe one of the sources (XID 647) with the laser guide star facility; however, due to technical problems, these observations were canceled. Of the remaining three sources, two have IR-red excesses, XIDs 277 and 580, and one, XID 57, was not detected at 24 $\mu$m despite a very red optical/near-IR color ($R - K = 6.56$), and hence is not included in the sample discussed in this paper.

For these sources we used SINFONI in the $0.25''$ spatial resolution mode, which provides a field of view of $8'' \times 8''$. The $H + K$ grism, which provides a wavelength coverage of 1.45–2.45 $\mu$m and a resolution of $R \sim 1500$, was used. The total exposure time was 3 hr for XID 580 and 2.7 hr for XID 277. In each case, a square dithering pattern with $4''$ offsets was performed so that the source was always in the field of view. This pattern was repeated 4 times.

Data were reduced using the official ESO SINFONI pipeline v1.9.4.[12] The SINFONI data reduction cookbook,[13] provided by the Paranal Science Operations group was followed. Briefly, raw data were first cleaned to remove bad lines created by the presence of hot pixels in the bias region. Then data are bias-removed and flat-fielded. Wavelength calibration was performed using arc lamps. Distortions were corrected using the provided wavelength maps. Finally, a data cube was reconstructed using the sinfo_rec_jitter routine. Flux calibration and removal of telluric features was performed using a standard star, typically a solar analog, observed within 2 hr of each science observation. Cube visualization and extraction of a two-dimensional pseudo-slit was done using the QFitsView tool.[14] Extraction of the one-dimensional spectrum, smoothing and flux calibration were performed using standard IRAF tools.

#### 2.4.2. MOIRCS Data

Source XID 322 was observed using the MOIRCS near-IR multi-object spectrograph mounted at the Subaru telescope on the night of 2008 December 18. MOIRCS was used in its multi-object mask mode, in order to use a sample of nearby bright stars to do the source acquisition. The *HK*500 grism, which provides a resolution of ~700 in the 1.3–2.5 $\mu$m wavelength range, was used. Ten-minute individual integrations were performed, after which the source was dithered by $3''$ along the slit following a standard ABBA routine in order to allow for an accurate sky subtraction. The total exposure time was 3 hr. Data reduction was done using the IDL-based MOIRCSMOSRED package created by Youichi Ohyama. Basic steps include extraction of the slit spectrum, sky-subtraction, flat fielding, flexure correction, co-adding of individual AB spectra to finally combine the resulting sky-subtracted spectra. Wavelength calibration was performed using OH sky-lines as reference and flux calibration was based on observations of HD20758, a G2V star, taken during the same night.

### 2.5. Photometric Redshifts

In order to obtain highly accurate photometric redshifts for all of the optically detected sources in the region of the ECDF-S, we obtained 18 medium-band images of the field. Our deep medium-band Subaru imaging reaches $R_{AB} \sim 26$, 2 magnitudes deeper than previous CDF-S medium-band imaging (COMBO-17 reaches $R_{AB} \sim 24$ with 12 medium-band filters and 10% accuracy; Wolf et al. 2004), and provides accurate redshifts (~1% accuracy) and detailed spectral energy distributions for $\geqslant$90% of the detected X-ray sources. The Subaru images reach nearly all of the X-ray-selected AGNs. The greater number of filters and their even spacing give an effective spectral resolution of $R = \lambda/\Delta\lambda \sim 23$ (Taniguchi 2004). The catalog was created using the deep BVR image for detection (Gawiser et al. 2006a), and contains roughly 60,000 sources with detailed spectral energy distribution. The catalog includes color-matched photometry from all 18 medium bands, in addition fluxes from the optical and near-IR ground based imaging (see Taylor et al. 2009 for more details on the broadband data). Details of the medium-band data reduction and characteristics are provided in C. Cardamone et al. (2009, in preparation).

In order to obtain accurate photometric redshifts, we used Easy and Accurate Zphot from Yale (EAZY), a program optimized to provide high quality redshifts over $0 < z < 4$ (Brammer et al. 2008). EAZY is a new user friendly, full featured redshift fitting code, including a user-friendly interface based on HyperZ (Bolzonella et al. 2000) and the use of priors (e.g., Benítez 2000). The template set and the magnitude priors are based on semi-analytical models which are complete to very faint magnitudes rather than highly biased spectroscopic samples, and so are particularly useful for samples of objects

[11] Available at http://www.eso.org/science/goods/spectroscopy/CDFS_Mastercat/

[12] The SINFONI pipeline can be found at http://www.eso.org/sci/data-processing/software/pipelines/sinfoni/sinfo-pipe-recipes.html.

[13] http://www.eso.org/sci/facilities/paranal/instruments/sinfoni/doc/

[14] Available at http://www.mpe.mpg.de/~ott/QFitsView/.

such as our optically faint mid-IR-selected sources, where complete spectroscopic calibration samples are not available. Further, EAZY introduces a template error function to account for wavelength-dependent template mismatch rather than relying on minimizing the scatter between photometric and spectroscopic redshifts of the subsample of sources bright enough to have spectroscopic redshifts. EAZY allows for linear combinations of the templates sets. We make use of this feature including an additional broad-line AGN template when fitting the X-ray sources. EAZY assigns each object a redshift by marginalizing over the full posterior probability distribution rather than maximizing the likelihood.

We compute the photometric redshifts for the sources detected in the combined BVR image using the default EAZY parameters, adopting the default template error function and *R*-band photometric prior, and including the optical and near-IR ground based coverage from the MUSYC survey (Taylor et al. 2009) in addition to our medium-band data. We find a median $\Delta z/(1+z)$ of 0.01 for all sources with spectroscopic redshifts out to $z \sim 5$. Limiting ourselves to the subsample of X-ray sources, we do only slightly worse, $\Delta z/(1+z) = 0.011$, but the fraction of outliers doubles to 20%. Overall, for $\Delta z/(1+z)$, this is a factor of 3 better than is currently done using broadband data (Brammer et al. 2008). We find good quality photometric redshifts ($q_z < 1$; Brammer et al. 2008) down to *R*-band magnitude of AB = 26 for 60% of the sample. For many of the remaining sources poor fits are obtained because the photometry is too uncertain, due to faintness of the sources, or intrinsic variability in the source over the time period of which the photometry was taken (Salvato et al. 2009). There are also cases where the intrinsic spectral energy distribution (SED) may not be matched by those provided in the template set or degeneracies in color-$z$ space can result in multiple peaks in the redshift-probability distribution. If no restriction in the quality parameter, $q_z$, is used the statistical quality of the photometric redshifts degrades only slightly, to $\Delta z/(1+z) = 0.016$ with an outlier fraction of 27%. Overall, with medium-band photometry, we have achieved highly accurate photometric redshifts for the majority of the sources in the ECDF-S down to very faint magnitudes.

## 3. OPTICAL/MID-IR SELECTION OF CT AGN CANDIDATES

X-ray observations have been very efficient in finding unobscured and moderately obscured AGNs up to high redshifts and low luminosities (e.g., Brandt & Hasinger 2005). However, highly obscured, particularly Compton-thick AGNs, have been significantly excluded even from the deep Chandra and XMM-Newton surveys. Because most of the radiation absorbed at X-ray and UV wavelengths is then re-emitted in the mid- and far-IR, recent studies at these energies, mostly taking advantage of *Spitzer* observations, have been very successful in finding heavily obscured AGN candidates missed by X-ray selection up to high redshifts (Daddi et al. 2007; Alexander et al. 2008; Donley et al. 2008; Fiore et al. 2008).

In particular, Fiore et al. (2008) presented a selection method based on the 24 $\mu$m to *R*-band flux ratio and $R - K$ color; specifically, $f_{24}/f_R > 1000$ and $R - K > 4.5$ (Vega). According to simulations based on stacking of the X-ray signal, they estimate the fraction of heavily obscured AGN in this sample to be greater than 80% (Fiore et al. 2008, 2009). Similarly, Daddi et al. (2007) found a large number of CT AGN candidates by selecting sources which show a significant excess in the star formation rate measured from IR light, compared to the value derived in the ultraviolet. However, Murphy et al. (2009) showed, using mid-IR spectroscopy and adding far-IR photometric data for the sources selected using the Daddi et al. (2007) method, that in only ~30% of the cases the observed mid-IR excess was due to the presence of an AGN, while in the majority of the sources the presence of strong aromatic PAH features explained the discrepancy in the derived star formation rates.

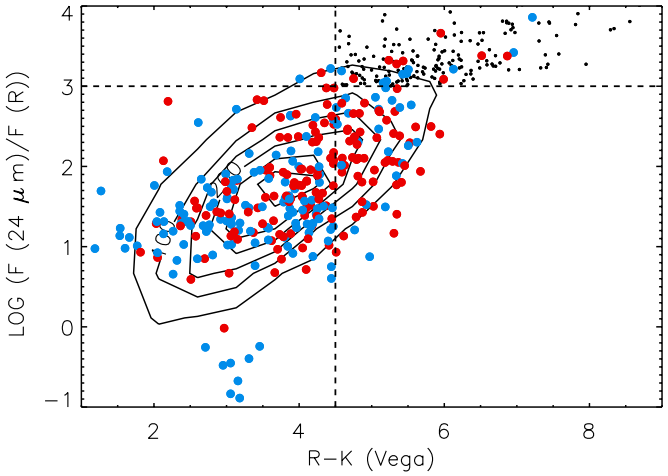


**Figure 1.** Ratio of 24 $\mu$m to *R*-band flux density as a function of $R - K$ color. Contours show the location of all the MIPS-selected sources. Red circles show the location of X-ray sources with HR (define as $(H - S)/(H + S)$, where *S* and *H* are the background-subtracted counts in the soft and hard bands, respectively) greater than −0.3, while blue circles have HR < −0.3. Small black circles show the 193 sources in the IR-red excess region that were not detected individually in X-rays. While there is no clear trend of HR with optical ($R - K$) color, most of the X-ray hard sources also have large $R - K$ colors.

(A color version of this figure is available in the online journal.)

We applied the "infrared-red" selection criteria of Fiore et al. (2008) to the MIPS-selected sources in the ECDF-S to select CT AGN candidates, as shown in Figure 1. Of the 7201 24 $\mu$m sources detected in the FIDEL observations to a flux limit of ~35 $\mu$Jy, 211 (~3%) satisfy the $f_{24}/f_R > 1000$ and $R - K > 4.5$ cuts. Of the 651 X-ray-detected sources in the Virani et al. (2006) catalog, 18 are found in this region, ~2.8%, a similar fraction as in the general population. The fraction of IR-red sources with a direct X-ray detection is ~9%, smaller than the 16% reported by Fiore et al. (2008) for the CDF-S observations, and significantly smaller than the fraction of direct X-ray detections in the COSMOS field (40%; Fiore et al. 2009). As can be seen in Figure 1, the typical value of $f_{24}/f_R$ for the ECDF-S sources is ~50–100, while $< R - K > \sim 3.5$, so the IR excesses are extreme, making them good candidates to be heavily obscured AGNs.

## 4. X-RAY DETECTED AGN

A total of 18 sources in the IR-red excess region were significantly detected individually in X-rays and included in the catalog of Virani et al. (2006). In addition, six more sources were detected in the 2 Ms Chandra observations covering the central CDFS region (Luo et al. 2008); two of the latter sources were included in the Lehmer et al. (2005) catalog, but were not reported by Virani et al. (2006). Four of these six sources were not included in the Alexander et al. (2003) catalog, indicating that they were very faint in X-rays and only significantly detected with the additional 1 Ms of data.

For comparison, Fiore et al. (2008) report that the same number of IR-red excess sources, 18, were directly detected in

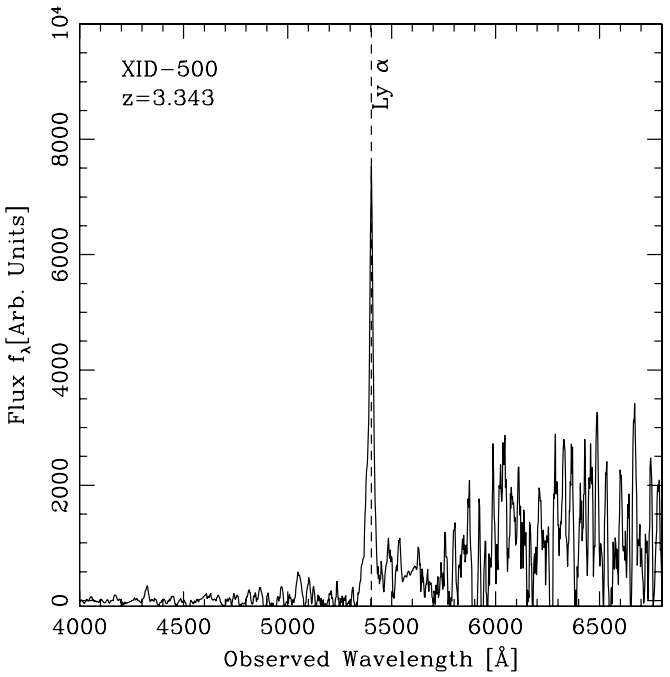


**Figure 2.** Optical spectrum of X-ray source 500 obtained using VLT/VIMOS (Treister et al. 2009b). Wavelength is shown in the observed frame. The redshift for this source is $z = 3.343$, identifying the strong emission line at ∼5400 Å as Ly$\alpha$, which is supported by the significant continuum decrement blueward of this line. The photometric redshift for this source is $1.75 \pm 0.1$ (99% confidence level), but with a very bad $\chi^2$. The closest identification matching the photometric redshift and the observed emission line is [CIII]1909 Å at $z = 1.83$; however, if this is the case, CIV at observed frame 4383 Å should also be visible. Hence, most likely the photometric redshift is wrong in this case.

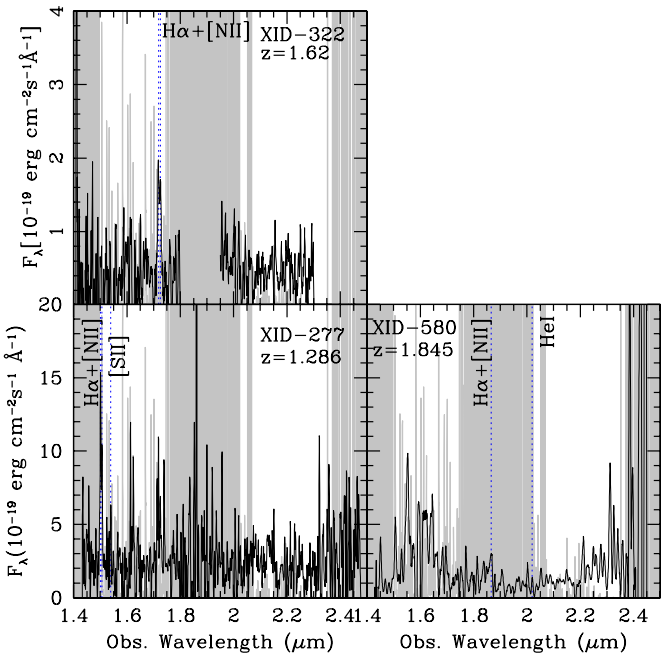


**Figure 3.** Near-IR spectra for three X-ray-detected IR-red excess sources in the ECDF-S. Wavelength is shown in the observed frame. Shaded wavelengths show spectral regions affected by low atmospheric transmission and OH sky lines (Rousselot et al. 2000). These spectra were obtained from VLT/SINFONI (XID-277 and XID-580) and Subaru/MOIRCS (XID-322).

(A color version of this figure is available in the online journal.)

X-rays and included in the 1 Ms Chandra catalog, with four more marginally detected. This can be expected by the combination of deeper X-ray data (by a factor of 4) and smaller area (by a factor of ∼7). Also, an important factor is the difference in depth of the *K*-band image used in their analysis. While the MUSYC ECDF-S images reach a magnitude limit of $K \simeq 20.2$, the GOODS-MUSIC catalogs reach almost two magnitudes deeper (Grazian et al. 2006).

After an extensive archival search, we found optical spectroscopy for two sources in our X-ray-detected sample, namely XIDs 480 and 500. Source XID480 is an intriguing source. Its redshift, $z = 1.603$, was securely measured by Szokoly et al. (2004) based on deep VLT/FORS1-FORS2 observations. These authors classified XID 480 as a QSO-1, based on the soft X-ray spectrum. However, only narrow emission lines are present in the optical spectrum. From X-ray spectral fitting (Treister et al. 2009b), we found that $N_{\rm H} = 2 \times 10^{22}$ cm$^{-2}$, consistent with the observed hardness ratio. Hence, this source is at the unobscured/obscured AGN boundary, which explains the discrepancy between the observed soft X-ray spectrum and the red optical/near-IR colors. Source XID 500 was observed by VLT/VIMOS as part of our MUSYC identification program (Treister et al. 2009b). The optical spectrum of this source is shown in Figure 2. The spectroscopic redshift for this source is 3.343, based on a strong narrow emission line at 5402 Å identified as Ly$\alpha$. In support of this interpretation, a strong decrement in the continuum is observed blueward of this line, while the continuum is clearly detected on the red side.

The near-IR spectra of sources 277 and 580 can be seen in Figure 3. The redshift of XID 277 is secured by the presence of a strong emission line, which is marginally resolved at the SINFONI resolution and consistent with the wavelengths of H$\alpha$ and [N II] at a redshift of 1.286. In addition, a weak [S II] line is present in the data. For XID 580, no obvious emission line is detected. However, on further inspection, two weak emission lines are found at wavelengths of 1.866 and 2.08 microns. These lines could be identified as H$\alpha$+[N II] and He I, respectively, at a redshift of 1.845. The weak detection of these lines can be explained by their location in a spectral region with very low atmospheric transmission. The main feature in the near-IR spectrum of XID 322 is a strong emission line at 1.722 microns. At the resolution of our setup, this line is barely resolved into two peaks, the largest one at 1.7179 $\mu$m and a smaller one at 1.7257 microns. This is consistent with H$\alpha$ and [N II] at a redshift of 1.621. No other feature is visible in this spectrum.

The redshift distribution for the IR-red excess sources detected in X-rays, including both photometric and spectroscopic measurements, is shown in Figure 4. The average redshift for our sample is 2.37 (median = 1.85), larger than the value of $1.55 \pm 0.53$ found by Fiore et al. (2009) for similar sources in the COSMOS field. This is most likely due to the much brighter 24 $\mu$m flux limit of their sample. Indeed, Fiore et al. (2008) reported an average redshift of 2.1 in the deeper CDFS observations. Similarly, Georgantopoulos et al. (2008) estimated an average redshift of ∼2 for similar sources in the Chandra Deep Field North. For our sample, the minimum redshift is 1.286 (XID 277) and the maximum is 4.65 (XID 303), although the latter is only a photometric redshift.

### *4.1. X-ray Properties*

Automated X-ray spectral fitting was performed for the sources in the ECDF-S using the Yaxx[15] software. An absorbed power law was assumed for all sources. For the two brightest

[15] Available at http://cxc.harvard.edu/contrib/yaxx/.

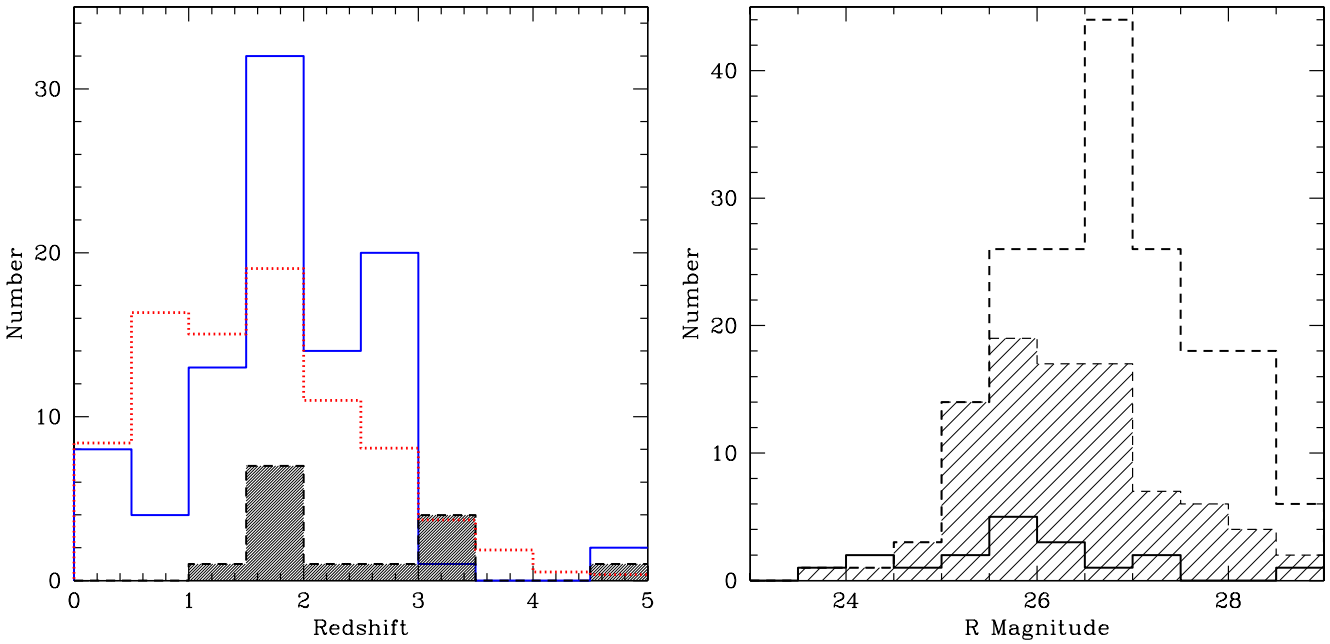


**Figure 4.** Left panel: redshift distribution for the 24 $\mu$m-selected sources in the ECDF-S. The solid histogram shows the distribution for the sources not detected in X-rays, while the dashed hatched histogram considers only the X-ray-detected sources. A K–S test shows that the hypothesis that these two distributions were drawn from the same parent distribution is refuted at the 84% confidence level. The dotted histogram shows the slightly lower redshift distribution (divided by 1000) for all the sources with a 24 $\mu$m detection and a measured photometric redshift in the ECDF-S. Right panel: distribution of *R*-band magnitude for the IR-red excess sources detected in X-rays (solid histogram), those not detected in X-rays (dashed histogram) and all sources with a measured photometric redshift (hatched histogram). Not surprisingly, spectroscopic and photometric redshifts are available preferentially for the optically brightest sources. In addition, X-ray-detected sources are brighter in the optical than the non-X-ray-detected ones.

(A color version of this figure is available in the online journal.)

sources, XID 480 and 284, with more than 200 background-subtracted counts, the spectral slope and amount of absorption were fitted simultaneously. In both the cases, the observed spectral slope is consistent with the fiducial $\Gamma = 1.9$ value (Nandra et al. 1997). For fainter sources, the spectral slope was fixed to $\Gamma = 1.9$ and only the amount of absorption was fitted. For sources in which the number of X-ray counts is even smaller (<80 counts), it is not possible to perform spectral fitting. In those cases, we use the hardness ratio (HR), defined as the ratio between the difference in counts in the hard and soft counts and their sum; the amount of absorption can be estimated from the HR by comparing the observed value with the expected counts for an intrinsic obscured power law with $\Gamma = 1.9$ at the redshift of the source and folding in the response of Chandra/ACIS. Because the same intrinsic spectral slope is assumed by the HR and spectral fitting methods, consistent results are obtained. The observed HR values and the corresponding calculated $N_{\rm H}$ for our X-ray-detected sample are shown in Figure 5.

From our derived $N_{\rm H}$ values we found two sources (13%) with $N_{\rm H} < 10^{22}$ cm$^{-2}$, i.e., unobscured AGNs, 11 (73%) with $10^{22} < N_{\rm H} < 10^{24}$ cm$^{-2}$ (moderately obscured sources), and two Compton-thick AGNs. The ratio of obscured to unobscured AGNs in this sample, 13:2, is significantly higher than the average value of ∼3–4:1 found in deep surveys with no color cut (e.g., Treister et al. 2004). Furthermore, all the sources in this sample have $L_X > 10^{43}$ erg s$^{-1}$. Due to the strong dependence of the fraction of obscured AGNs on luminosity (e.g., Ueda et al. 2003; Steffen et al. 2003; Barger et al. 2005), the fraction of obscured to unobscured sources is expected to be significantly lower (∼1:2 at this luminosity; Treister et al. 2009b), making the excess in the relative number of obscured AGN more significant.

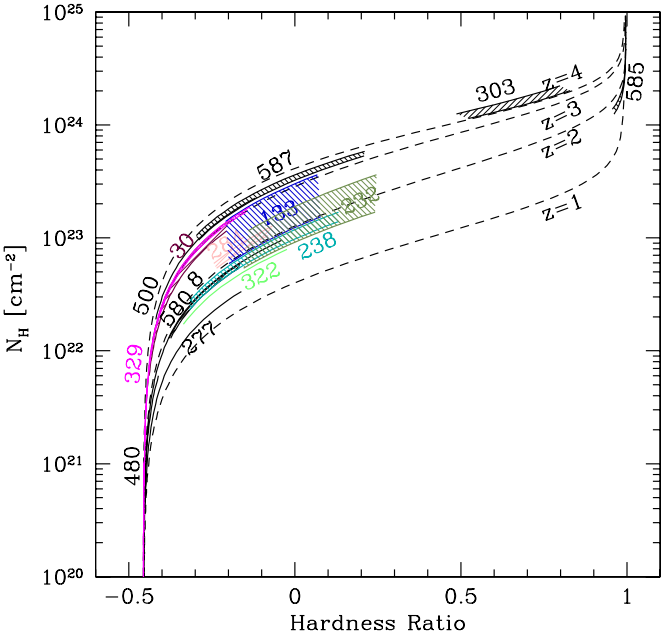


**Figure 5.** Neutral hydrogen column density ($N_H$) as a function of hardness ratio for the 15 X-ray sources with either spectroscopic or photometric redshifts. $N_{\rm H}$ was calculated from spectral fitting for the X-ray brightest sources and from the HR for the remaining ones. For the two brightest sources, XID 480 and 284 we measured $\Gamma = 2.5 \pm 0.6$ and $1.7 \pm 0.7$ respectively. For the remaining sources, we assumed an intrinsic power-law spectrum with $\Gamma = 1.9$ at the observed redshift of the source and correcting for galactic absorption. In general, these are very obscured sources in X-rays, with $N_{\rm H} > 10^{22}$ cm$^{-2}$, and two have Compton-thick absorption levels (XID 303 and 585).

(A color version of this figure is available in the online journal.)

This confirms that the IR-red excess selection preferentially find obscured sources, although only a small fraction of this sample reaches Compton-thick absorption levels.

## 5. X-RAY UNDETECTED CT AGN CANDIDATES

As was mentioned in Section 3, a total of 211 24 $\mu$m sources in the ECDF-S were found in the IR-red excess region, 18 of them individually detected in X-rays and included in the catalog of Virani et al. (2006). Of the remaining sources, eight were detected in X-rays either by Lehmer et al. (2005) or in the deeper catalogs of Alexander et al. (2003) and Luo et al. (2008). Here we focus on the 185 X-ray-undetected obscured-AGN candidates. According to Fiore et al. (2008), the vast majority of these sources should be heavily obscured, even Compton-thick, AGNs, in which the combination of photoelectric absorption and Compton scattering explains the lack of X-ray detection. In order to test this hypothesis, we study the nature of these sources at many wavelengths through X-ray stacking, optical/mid-IR spectral analysis and IRAC colors.

### 5.1. Photometric Redshift Distribution

Contrary to the situation for the X-ray-detected sources, where four sources had a measured spectroscopic redshift, none of the 185 X-ray-undetected sources have a spectroscopy redshift. Hence, redshifts for these sources will be based on photometric measurements only. Because of the faintness of the optical/near-IR counterparts, accurate photometric redshifts are available for only 90 (49%) sources. The remaining 95 sources were not detected in the deep BVR image and hence it was not possible to compute photometric redshifts. The redshift distribution of these sources is shown in Figure 4.

The vast majority of the mid-IR-selected sources have photometric redshifts greater than one, with a median of 1.9, a significantly smaller value than for the X-ray-detected sources. Performing a Kolmogorov–Smirnov (K–S) test to these two distributions we found that the hypothesis that they were drawn from the same parent distribution is marginally rejected at a 84% confidence level. This small discrepancy can be due to the relatively large fraction of X-ray sources at $z > 3$, in contrast with the strong drop at that redshift for the X-ray-undetected sample. We also found that X-ray-detected sources are in general brighter than the X-ray-undetected ones in both the 24 $\mu$m and $R$ bands, as can be seen in Figure 4. A K–S comparing the $R$-band magnitudes for the X-ray-detected and undetected sources found that the hypothesis that they are drawn from the same parent distribution is rejected with >99% confidence. This difference in optical magnitude explains why the X-ray-detected sample extends to higher redshifts. Furthermore, as mentioned before, the redshift completeness for the IR-red excess sources not detected in X-rays is 49%, while for the X-ray-detected sources is 83%, thus supporting the idea that the optical brightness explains the difference in redshift distribution.

Compared to the general distribution of optically detected sources in the ECDF-S, the IR-red excess sources are found at significantly higher redshifts. This may be an effect of the selection, namely the $f(24\ \mu\mathrm{m})/f(R) > 1000$ requirement. Because for obscured AGN the rest-frame optical/UV light is dominated by the host galaxy (e.g., Treister et al. 2005 and references therein), the $f(24\ \mu\mathrm{m})/f(R)$ is essentially a measurement of the AGN-to-host galaxy luminosity ratio. Hence, the fact that the 24 $\mu$m-selected sources are found mainly at $z > 1$ is a consequence of the available volume for high-luminosity sources. Furthermore, these sources do not have local analogs since even the most luminous nearby star-forming galaxies cannot reach such high $f_{24\ \mu\mathrm{m}}/f_R$ ratios (Dey et al. 2008). The high-redshift dropoff at $z \sim 3$ can be explained by the faintness of the optical counterparts at such redshifts, thus making the determination of photometric redshifts very hard.

### 5.2. X-ray Stacking

Thanks to its very low background, Chandra data can be efficiently stacked in order to study the average X-ray properties of a sample of individually undetected sources, thus achieving an effective exposure time of many megaseconds (e.g., Brandt et al. 2001). In order to perform X-ray stacking we used both the web-based CSTACK code[16] developed by T. Miyaji and our own scripts, which are based on CIAO (Fruscione et al. 2006) version 4.1. In all the cases, we found consistent results using these two codes. Stacking was done using the final unbinned mosaics of ECDF-S Chandra observations, which were produced as described by Virani et al. (2006). The stacking was performed in two bands independently: soft (0.5–2 keV) and hard (2–8 keV).

We started from the sample of 185 24 $\mu$m-selected sources in the ECDF-S not detected in X-rays. To avoid possible contamination and enable a more accurate background measurement, we excluded 46 sources for which there was a detected X-ray source closer than 15″. After co-adding the remaining sources the effective exposure time was ∼30 Ms or ∼one year. The stacked image in both the soft and hard bands is shown in Figure 6. Total source counts were measured in a 3″ radius circle. The background properties were estimated in two different ways: by using an annulus with a 7″ inner radius and 15″ outer radius and by performing photometry in random 3″ circles outside the central region. The results from both methods are roughly consistent with each other. We measured a total of 68 and 89 background-subtracted counts in the soft and hard bands. The background standard deviations are 14.1 and 32.8 counts, respectively, which corresponds to a signal to noise of ∼4.8 in the soft band and ∼2.6 in the hard band. The significance of these detections was established by performing 500 independent Monte Carlo simulations, stacking 139 random positions in the field, thus having the same effective exposure time and noise properties as the stacking of the 24 $\mu$m-selected sources. By studying the distribution of central background-subtracted counts in these simulations we found that, as expected, they are consistent with a Gaussian distribution with standard deviations of 17 and 22 counts in the soft and hard bands, respectively. This indicates that the signal detected for the 24 $\mu$m-selected sources is significant at the $\sim 4\sigma$ level in each band. The latter measurement is more robust because it is based on 500 independent determinations, compared to the 20 3″ circles used in the method described previously, hence significantly reducing the effects of the faint undetected X-ray sources in the distribution of background counts.

In order to convert count rates into fluxes we used the Portable, Interactive Multi-Mission Simulator (PIMMS) tool.[17] Assuming the corresponding Chandra/ACIS response functions, an intrinsic power-law spectrum with $\Gamma = 1.9$, Galactic absorption of $8 \times 10^{19}$ cm$^{-2}$ (Kalberla et al. 2005), and intrinsic absorption of $10^{24}$ cm$^{-2}$ at $z = 2$, we found conversion factors from counts/second to erg cm$^{-2}$ s$^{-1}$ of $6.5 \times 10^{-12}$ in the soft band and $2.6 \times 10^{-11}$ for the hard band. Hence, the average observed

[16] http://cstack.ucsd.edu/

[17] Web version available at http://heasarc.gsfc.nasa.gov/Tools/w3pimms.html.

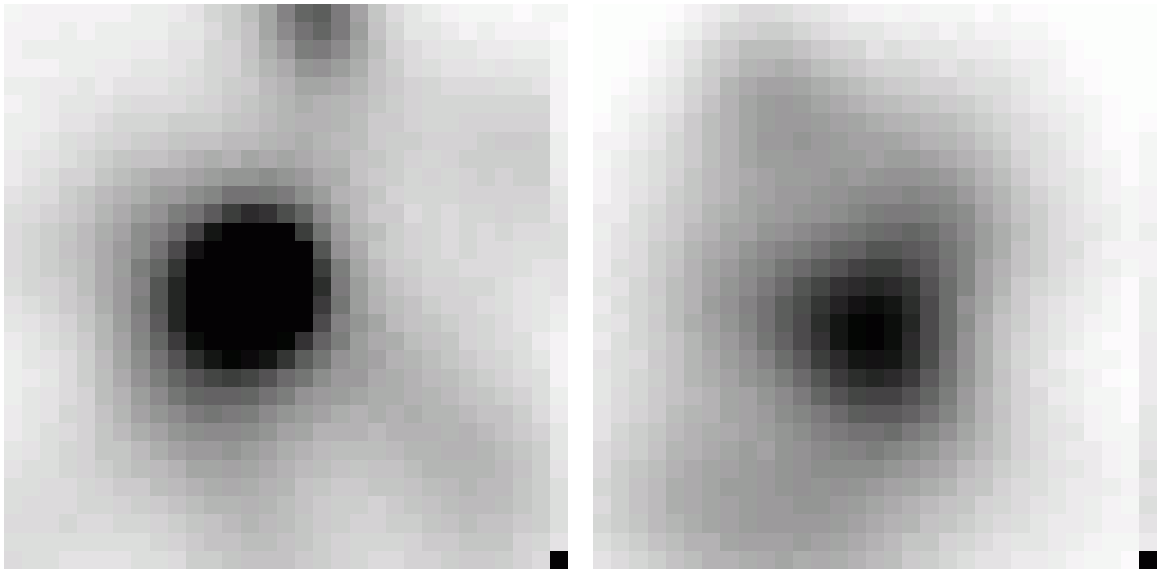

**Figure 6.** X-ray stacking of 129 sources not detected individually by Chandra in the soft (0.5–2 keV; left panel) and hard (2–8 keV; right panel) bands. The equivalent exposure time is ∼30 Ms. A significant detection, $\sim 4\sigma$, is found in each band independently. The total background-subtracted counts are 68.1 in the soft band and 86.5 in the hard band, which correspond to average fluxes of ∼2 and $\sim 8 \times 10^{-17}$ erg cm$^{-2}$ s$^{-1}$, respectively.

(A color version of this figure is available in the online journal.)

X-ray fluxes for the 24 $\mu$m-selected sources are $\sim 2.1 \times 10^{-17}$ erg cm$^{-2}$ s$^{-1}$ in the soft band and $\sim 8 \times 10^{-17}$ erg cm$^{-2}$ s$^{-1}$ in the hard band. If instead a lower column density, $2 \times 10^{23}$ cm$^{-2}$, is assumed, the fluxes in the soft and hard bands are reduced by 17% and 20%, respectively. Similarly, if a $z = 1$ is assumed instead for a $N_{\rm H} = 10^{24}$ cm$^{-2}$ spectrum the conversion for the hard band is increased by 27%, while if $z = 3$ is used the conversion is decreased by 13%. We can hence conclude that the uncertainties due to the assumption of an average spectral shape for the counts-to-flux conversion generate uncertainties smaller than ∼30%.

The HR for the stacked X-ray signal is $0.13 \pm 0.06$. For comparison, for the sources individually detected in X-rays we found an average HR of $-0.23 \pm 0.01$, significantly softer than the value for the X-ray-undetected sample. This higher HR suggests the presence of more obscured sources in the X-ray-undetected sample. Converting directly this HR into a $N_{\rm H}$ for a intrinsic power-law spectrum with $\Gamma = 1.9$ and the average redshift of our sample, $z \simeq 2$, we find that $N_{\rm H} \simeq 1.8 \times 10^{23}$ cm$^{-2}$. If instead the extreme values of $z = 1$ and $z = 3$ are considered we obtain values of $N_{\rm H} = 5 \times 10^{22}$ and $4 \times 10^{23}$ cm$^{-2}$ respectively, i.e., a uncertainty of $\sim 2\times$ can be expected due to the redshift distribution of our sources. However, and more importantly, we note that the observed HR could be significantly affected by the presence of X-ray emission from non-AGN galaxies, which have in general a softer spectrum (e.g., Fabbiano 1989). In order to estimate the fraction of obscured AGNs relative to star-forming galaxies in a stacked sample, Fiore et al. (2009) performed simulations combining these two types of sources to match the observed HR. These simulations take into account the redshift distribution of our sources. Converting our observed HR into the bands used in their work (0.3–1.5 and 1.5–6 keV) we find that the fraction of heavily obscured AGNs with $N_{\rm H} > 10^{23}$ cm$^{-2}$ is ∼90%.

To understand the effects of the sources without either a photometric or spectroscopic redshift determination on our results we stacked separately the 90 sources with a redshift measurement. A total of 25 and 31 background-subtracted counts were detected in the soft and hard bands, respectively. The HR derived from these detections is $0.11 \pm 0.16$, i.e., in very good agreement with the value found for the whole sample. This indicates that while sources without a measured redshift can have a different redshift distribution, this does not affect our results significantly. Similarly, splitting the sample with redshift measurements at $z = 2$, roughly the median of the distribution, we detected 18 (soft band) and 27 (hard band) background-subtracted counts for sources at $z < 2$, while no significant detection was obtained for the $z > 2$ sample. The HR for the $z < 2$ sample is $0.2 \pm 0.18$, slightly larger but consistent with the value obtained for the whole sample.

To further study the possible effects of the spread in redshift of our sample we also performed X-ray stacking in the approximate rest-frame, i.e., multiplying each observed photon energy by $1 + z$ before stacking. (This is not strictly correct since one should correct the incident photon energy rather than the observed photon energy. However, for the Chandra ACIS detectors, as for most X-ray detectors with modest energy resolution, a delta function of incident photons is redistributed over a broad range of energies and the response matrix cannot be inverted in a stable or unique way.) This pseudo-rest-frame stacking can be done only for the 90 sources with redshift measurements, which is roughly half the sample. Excluding the sources closer than $15''$ to a individually detected X-ray source further reduces our sample to 63 sources. We perform this X-ray stacking in four rest-frame bands: 1.5–5, 5–10, 10–15, and 15–24 keV. In the first three bands, we obtained a signal-to-noise ratio greater than ∼2, while there is no significant detection in the last band, most likely due to the rapid decrease in sensitivity of Chandra at high energies and the reduced number of sources at high redshift in our sample. These results are shown in Figure 7. In order to compare with sources with a known spectral shape, we also stacked the X-ray emission from the 15 IR-red excess sources individually detected in X-rays with a measured redshift. As described in Section 4.1, these sources are obscured AGN with an average $N_{\rm H} \simeq 10^{23}$ cm$^{-2}$. We also compare with the rest-frame X-ray spectrum of a luminous unobscured AGNs found

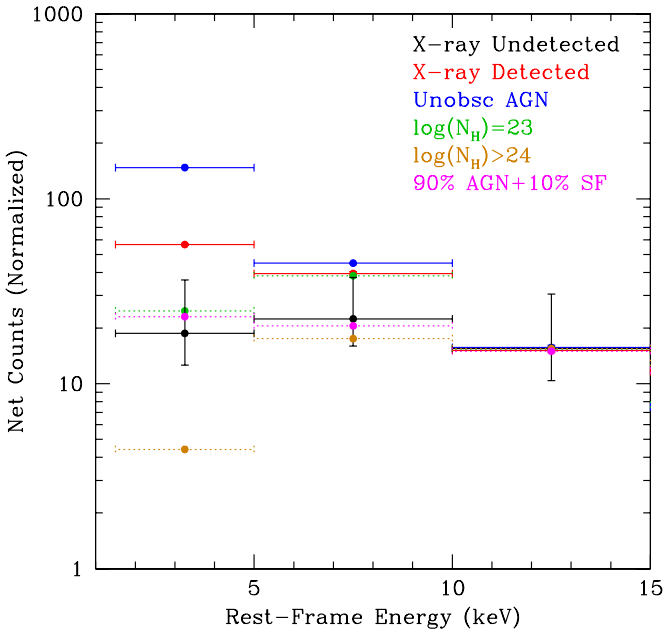


**Figure 7.** Spectrum resulting from X-ray stacking performed in the approximate rest-frame. The *black points* show the background-subtracted counts measured from the combination of 63 IR-red excess sources with measured redshifts that were individually undetected in X-rays, while the *red points* show the combined signal from the 15 X-ray-detected IR-red excess sources. The *blue points* show the spectrum of source XID-312, a luminous unobscured AGN in the ECDF-S at $z = 1.887$. The last two spectra were normalized to the measurement for the X-ray-undetected sources at 10–15 keV, where the emission should be more isotropic. The *green* and *brown* data points show the expected spectral shape for heavily obscured AGN with column densities of $N_{\rm H} = 10^{23}$ and $>10^{24}$ cm$^{-2}$ (see text for details). The *magenta* data points show the combined spectrum of a population of 90% CT AGN and 10% pure star-forming galaxies. The spectrum of the X-ray-undetected sources can be well explained by either an obscured AGN with $N_{\rm H} \gtrsim 10^{23}$ cm$^{-2}$ or a mixed population of Compton-thick AGN and star-forming galaxies.

(A color version of this figure is available in the online journal.)

in the same field, XID 312, which according to Treister et al. (2009b) has a redshift of 1.887 and hence covers the same rest-frame energy range as our IR-red excess sample. As expected, the X-ray spectrum of the IR-red excess sources is significantly harder than those of the X-ray-detected sources with similar optical/IR colors and a typical unobscured AGN.

To quantify the amount of absorption from the rest-frame X-ray stacked signal presented in Figure 7, we compute the X-ray spectra of a heavily obscured AGN with $N_{\rm H} = 10^{23}$ and $> 10^{24}$ cm$^{-2}$. For the latter, we incorporate the effects of Compton scattering, as described by Matt et al. (1999), and an Fe K$\alpha$ line at 6.4 keV with an equivalent width of 2 keV, typical of Compton-thick AGN (Gilli et al. 1999). Figure 7 shows that for the sample of 15 IR-red excess sources individually detected in X-rays, an $N_{\rm H}$ of $10^{23}$ cm$^{-2}$ explains the observed ratio of 5–10 to 10–15 keV flux; at lower energies, the contribution from less-obscured sources in this sample can explain the observed excess relative to the model predictions. In the case of the IR-red excess sources individually undetected in X-rays, the spectrum in the 1.5–15 keV range can be well explained both by an obscured AGN with $N_{\rm H} \gtrsim 10^{23}$ cm$^{-2}$ or by a mixed population of a majority of Compton-thick AGNs and star-forming galaxies, with the later providing most of the flux at E<5 keV. For example, in Figure 7 we show the resulting X-ray spectrum of combining a population of 90% CT AGNs with 10% pure star-forming galaxies. This is fully consistent with our results derived from the X-ray signal stacked in the observed frame presented above. Hence, we conclude that the redshift spread does not affect our conclusions and therefore in this work we focus on the observed-frame measurements in order to increase our sample and thus the significance of our results.

A possible dependence of the fraction of AGNs on mid-IR flux (and thus luminosity) for X-ray-selected sources was reported by Treister et al. (2006) and Brand et al. (2006). Hence, it is reasonable to expect a similar behavior for our 24 $\mu$m-selected sample. In order to test for this effect, we separated our sample in three bins based on 24 $\mu$m flux, with the number of sources chosen to guarantee a signal-to-noise ratio for the X-ray stacked signal greater than two. The brighter bin includes 34 sources with $268 < f_{24\,\mu{\rm m}}\ (\mu{\rm Jy}) < 1292$. The signal to noise of the stacked signal in the hard band is ∼2.9. For these sources, we measure an HR of $0.37 \pm 0.25$, which using the simulations of Fiore et al. (2009) corresponds to an AGN fraction of ∼95%. At intermediate 24 $\mu$m fluxes, we stacked 33 sources with $155 < f_{24\,\mu{\rm m}}\ (\mu{\rm Jy}) < 266$. The detection of the stacked signal in the hard band is 2.1. In this case, we found an HR of $-0.02 \pm 0.01$, or an AGN fraction of ∼80%. Similarly, for the faintest 72 sources, with $53 < f_{24\,\mu{\rm m}}\ (\mu{\rm Jy}) < 148$, we found that HR = $0.018 \pm 0.01$, which also corresponds to an AGN fraction of ∼80%, although in this case the hard-band detection is not significant ($\sigma < 2$). In conclusion, although we find a weak trend of AGN fraction with 24 $\mu$m flux, it is not a statistically significant result.

### 5.3. Optical/Mid-IR Spectral Fitting

Because in obscured AGNs the optical light is dominated by the host galaxy, it is feasible to study the stellar population in these sources. In order to do that, we fit the *UBVRIzJK* spectral energy distribution of our IR-red excess sources to an ensemble of model star formation histories based on a two-burst scenario (see e.g. Ferreras & Silk 2002; Schawinski et al. 2007; Kaviraj et al. 2007) using the stellar models of Maraston (2005). We allow the young burst to make up between 1% and 100% of the stellar mass and range freely in age up to the age of the old burst, which must be at least 500 Myr old. We vary the decay timescale of the young burst from 10 Myr (an instantaneous burst) to 5 Gyr (effectively constant SFR) and fix the metallicity of both components at the solar value. We apply a screen of dust using the extinction law of Calzetti et al. (2000) for starburst galaxies and allow the color excess $E(B-V)$ to vary from 0 to 2.8. An AGN component was not added since for these sources the amount of obscuration of the nuclear region should be large enough to completely absorb the UV and optical emission, in order to explain the red $R - K$ color. Only those sources with detections in sufficient bands to have at least one degree of freedom (six bands) are fitted. For the majority of sources where we do not have a spectroscopic redshift, we assume the photometric redshift to be the true redshift. We find that not all IR-red excess sources result in an acceptable value of the reduced $\chi^2$ statistic: of those sources with X-ray counterparts, 12 out of the 15 that have detections in at least six bands and a redshift measurement, have a reduced $\chi^2_{\rm r} < 3.84$.

The nature of the available data limits what we can infer about the star formation history of these sources. We are sampling the rest-frame UV and blue optical part of the spectrum and expect a large amount of extinction in the UV. We also only have broadband photometry; so as a result, we cannot constrain whether the current starburst that we do infer is an event in which most or all of the stellar mass is formed, or whether it is

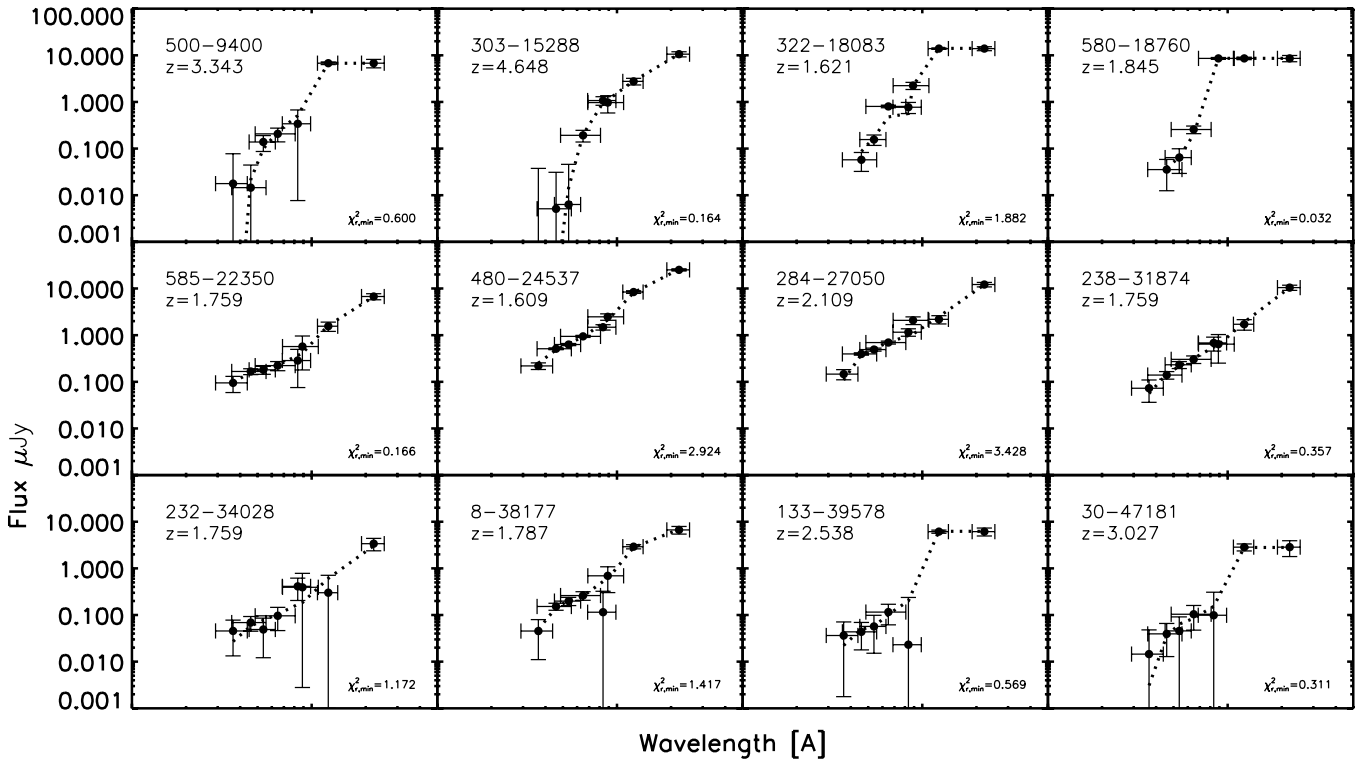


**Figure 8.** Spectral energy distributions for the 12 IR-red excess sources in the ECDF-S individually detected in X-rays with measured spectroscopic or photometric redshift and detections in at least six bands. *Circles with error bars* show the observed photometric fluxes in the *UBVRIzJHK* bands. *Dotted lines* show the fit to the rest-frame optical light using galaxy templates. The median stellar mass for this sample is $5 \times 10^{11}\ M_{\odot}$, while the average extinction is $E(B-V) = 0.6$.

a less substantial burst with younger ages and higher amounts of extinction. In Figure 8, we show the resulting UV-optical spectral fitting for the X-ray-detected sources. The median stellar mass for this sample is $4.6 \times 10^{11}\ M_{\odot}$, while the average extinction is $E(B-V) = 0.6$.

For our sample of IR-red excess sources not detected in X-rays, and requiring a redshift measurement and detection in at least six bands, we found acceptable fits for 60 out of 84 sources. The most likely explanation for the poor fits are inaccurate photometric redshifts. We marginalize over the nuisance parameters to investigate the stellar masses and levels of optical extinction inferred for our sample of IR-red excess sources. In general, they contain substantial stellar populations in an ongoing burst younger than 100 Myr and widely range in levels of optical extinction ($0 < E(B-V) < 1$).[18] The best-fit stellar masses range between $10^{9}$–$10^{12} M_{\odot}$ with a median stellar mass of $\sim 10^{11} M_{\odot}$. We caution that the typical uncertainties in the individual stellar masses after marginalization are on the order of a factor of 10. We further investigate the effects of the uncertainty in the photometric redshift derivation in our derived stellar masses and star formation histories, by varying the redshift within its $1\sigma$ allowed range while doing spectral fitting. We found that the dispersion in the stellar masses is on the order of 0.1 dex, which is substantially smaller than the typical errors on individual masses. Furthermore, the typical properties of the derived star formation histories are not affected. Hence, we conclude that for the sources with good spectral fits, the errors on the derived stellar masses and star formation histories are dominated by errors on the fluxes, in particular in the near-IR bands, and not by the photometric redshift errors.

[18] This range in $E(B-V)$ corresponds to $0 < A_V < 4.05$ assuming an $R_V = 4.05$ that the Calzetti et al. (2000) law uses.

In Figure 9, we show examples of spectral fitting for IR-red excess sources not detected in X-rays. We plot the histograms of the distributions of best-fit stellar masses and optical extinctions in Figure 10—the hashed histogram in each panel represents the sources individually detected in X-rays, while the solid histogram represents those without detections. We perform a K–S to determine whether the $E(B-V)$ and stellar mass distributions of the X-ray-detected and undetected IR-red excess sources are consistent with being drawn from the same parent population. We find that at the 90% confidence level, both distributions are consistent, and therefore no significant differences are found between the host galaxies of the X-ray-detected and undetected sources.

## 6. DISCUSSION

### 6.1. Near- and Mid-IR Colors

As it was shown in Section 5.2, the stacked X-ray signal for our 24 $\mu$m-selected sample indicates that most of these sources are consistent with being heavily obscured AGNs. In addition to the X-ray spectral shape, the rest-frame near and mid-IR colors provide important clues about the obscuration levels in these sources and the importance of the AGNs relative to the host galaxy. As expected from most dust re-emission models (e.g., Nenkova et al. 2002), the AGN spectrum at $\sim$3–10 $\mu$m is significantly affected by the amount of material in the line of sight (due to the effects of self-absorption), which should be related to the obscuration of the X-ray emission.

As can be seen in Figure 11, the distributions of $f_{24}/f_{8}$ flux ratios for X-ray-detected and undetected sources are significantly different. Indeed, performing a K–S test, we found that the hypothesis that these distributions were drawn from the same parent distribution is rejected at the >99.999% confidence

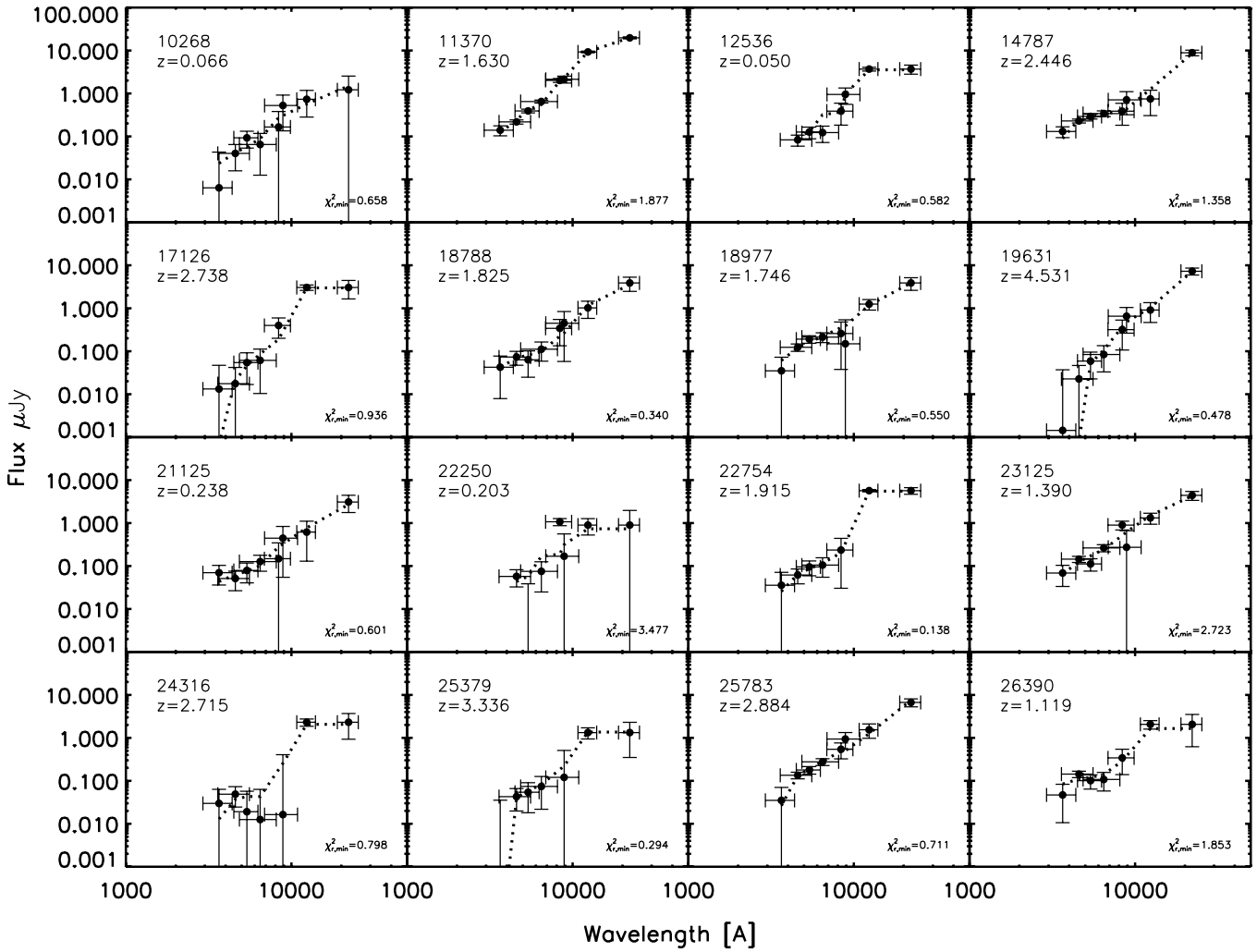


**Figure 9.** Spectral energy distributions for a random sample of 16 IR-red excess sources not detected in X-rays individually. Symbols are the same as in Figure 8. The mean stellar mass for the IR-red excess sources not detected in X-rays is $10^{11} M_{\odot}$, while the mean $E(B-V)$ is 0.4. Both the stellar mass and extinction are slightly lower but consistent with the values found for the X-ray-detected sources. In general, we found evidence for a substantial young stellar population, indicating that the host galaxies of most of these sources are experimenting significant moderately obscured star formations episodes.

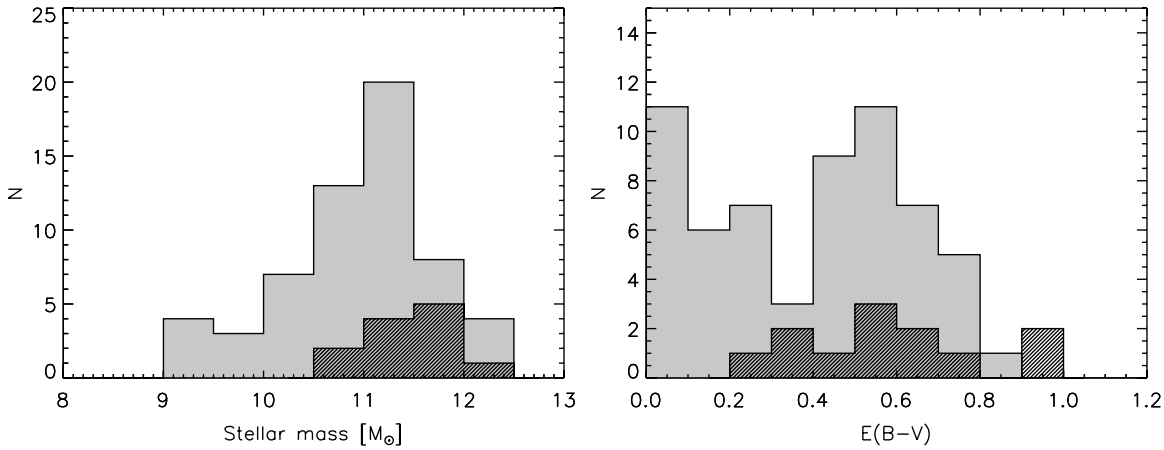


**Figure 10.** Left panel: distribution of stellar masses for the IR-red excess sources individually detected in X-rays (hatched histogram) and not detected in X-rays (solid histogram). The median values and distribution for these two samples are very similar. Indeed, a K–S test performed to these distributions indicate that they are consistent with being drawn from the same parent distribution at the 90% confidence level. Right panel: distribution of extinction in the host galaxy, as measured from template fitting to the rest-frame UV/optical light. Symbols are the same as in the left panel. In contrast to X-ray absorption, which measures mostly the AGN obscuration, no significant differences are found between these two samples. In summary, we did not find major differences between the host galaxies of the X-ray-detected and undetected sources.

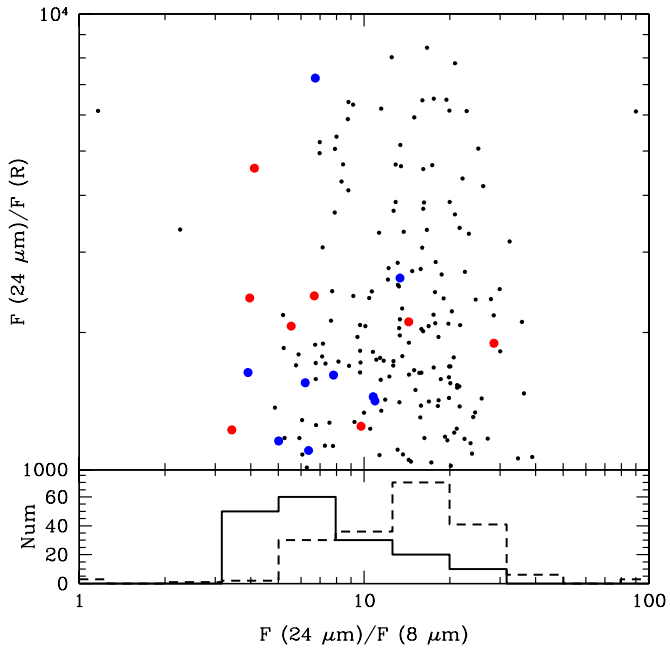


**Figure 11.** Upper panel: ratio of 24 $\mu$m to *R*-band flux density vs. 24 $\mu$m to 8 $\mu$m flux ratio for the 24 $\mu$m-selected AGN candidates in the ECDF-S. Same symbols as in Figure 1 are used. Lower panel: distribution of 24 $\mu$m–8 $\mu$m flux ratio for the X-ray-detected (solid histogram, increased by 10×) and undetected (dashed histogram) sources. A clear difference between the two distributions is seen, with X-ray-detected sources having much bluer colors.

(A color version of this figure is available in the online journal.)

level. The distribution of $f_{24}/f_8$ ratios indicate a much bluer mid-IR spectrum for the X-ray-detected sources. The average values of $f_{24}/f_8$ are 8.7 for the X-ray sources and 24.9 for the X-ray-undetected sources. At the typical redshift of our sources, these bands trace emission at rest-frame ∼8 and ∼3 microns. The dust re-emission models of Nenkova et al. (2008b) suggest that these observed values could be explained by the same intrinsic torus parameters and two different viewing angles. For example, for a torus model with $N = 10$ (number of equatorial clouds), $\sigma = 30$ (width of cloud's angular distribution), $Y = 30$ (ratio of outer to inner radii), $q = 2$ (exponent of cloud's radial distribution assuming a power law) and $\tau_v = 40$ (optical depth of an individual cloud; parameter definition given by Nenkova et al. 2008a), which are consistent with the models used by Nenkova et al. (2008b) to explain the mid-IR spectra of local Seyfert galaxies, the 8$\mu$ to 3$\mu$ flux ratios are consistent with the observed values for viewing angles of 30° for the X-ray-detected sample and 90° (edge-on) for the X-ray undetected sources. These parameters are mentioned just as an example. By studying a total of 19,939 torus models spanning a wide range of parameters we found that in ∼10% of them the resulting $f_{24}/f_8$ ratios are consistent with the observed values, taking into account the redshift distribution of our sources and assuming a viewing angle smaller than 30° for the X-ray-detected sources and greater than 70° for the undetected ones.

As shown in the sample of ultra-luminous IR galaxies presented by Armus et al. (2007), in their Figure 10, only a few sources reach values of the $f_{24}/f_8$ flux ratio as high as those observed in our sample of X-ray-undetected IR-red excess sources. Furthermore, those sources are mostly classified as LINERs, while using classification schemes based on optical emission lines (e.g., Kewley et al. 2006) they are found in the "composite" region, i.e. they can be explain by a combination of an AGN and strong star formation. Hence, we can conclude that the observed $f_{24}/f_8$ ratios in our X-ray-undetected sample strongly suggest the presence of a heavily obscured AGNs in the majority of them.

At the median redshift of our sample the *Spitzer* IRAC observations trace near-IR emission at ∼1$\mu$ to ∼3$\mu$. This spectral region is dominated by a combination of stellar light, AGN continuum and hot dust emission. There have been several studies of the IRAC properties of X-ray-selected AGNs (e.g., Barmby et al. 2006; Cardamone et al. 2008). One of the main conclusions of the work of Cardamone et al. (2008) is that AGN show a large spread in near-IR colors and thus the IRAC color–color AGN selection methods of Lacy et al. (2004) and Stern et al. (2005), which work very well to find luminous optically unobscured sources, are not particularly efficient in finding obscured/low-luminosity AGN. Figure 12 shows two combinations of IRAC color–color diagrams for the X-ray sources and 24 $\mu$m-selected AGN candidates in the ECDF-S. Interestingly, the X-ray-detected sources with $f_{24}/f_R > 1000$ and $R - K > 4.5$ fall inside the AGN regions of Lacy et al. (2004) and Stern et al. (2005). However, the vast majority of the X-ray-undetected IR-red excess sources are found outside the Stern et al. (2005) region and on the edge of the Lacy et al. (2004) locus.

As for the $f_{24}/f_8$ flux ratio, we also find in the IRAC colors significant differences between the X-ray-detected and undetected samples. In the IRAC case, most of the differences are found at longer wavelengths. In fact, we found very small differences in the [3.6]−[4.5] color (average [3.6]−[4.5] = 0.79 for X-ray sources and 0.69 for the X-ray-undetected sample), while significant differences can be seen in the [5.8]−[8] color (average of 0.99 for X-ray sources versus 0.5 for the X-ray undetected sample). As at longer wavelengths, these differences can be well explained by the effects of self-absorption of the dust re-emission. Using the Nenkova et al. (2008a) torus models, we found that for heavily absorbed sources the emission at wavelength shorter than ∼5 $\mu$m is dominated by stellar light, as the AGN re-emission is severely obscured. This explains why the 24 $\mu$m-selected sources not detected in X-rays fall in the same region of the [3.6]−[4.5] versus [5.8]−[8] diagram as inactive galaxies at $z > 2$ (Barmby et al. 2006). In the case of the X-ray-detected sources, the significant torus contribution in the observed-frame 8 $\mu$m band explains why these sources are displaced to the right in this diagram, so that they fall inside the Stern et al. (2005) diagram. A very similar effect can be seen in the right panel of Figure 12, where self-absorption can explain the observed difference in $f_8/f_{4.5}$ flux ratio.

The mid-IR colors of 24 $\mu$m-excess sources were also studied by Pope et al. (2008) in the GOODS-N field, to similar MIPS 24-$\mu$m depths. The first surprising result is that they found that >90% of their sources with $f_{24}/f_R > 1000$ also have $R - K > 4.5$. In contrast, we found that this fraction is 77% in our sample, while Fiore et al. (2008) report a fraction of ∼50%. One explanation mentioned by Pope et al. (2008) is that the fainter 24 $\mu$m sources have in general blue $R - K$ colors. However, in our sample we found that out of the 74 sources with $f_{24}/f_R > 1000$ and $R - K < 4.5$ only 8 have $f_{24\,\mu m} < 100\,\mu$Jy. Another possibility is that the different *K*-band magnitude limit of each sample can explain these discrepancies. While Pope et al. (2008) do not quote their flux limit in the *K* band, they mention that a large fraction (75 of 79, 95%) of the sources with $f_{24\,\mu m}/f_R > 1000$ are detected in the *K* band. Similarly, the *K*-band imaging in the GOODS-S region used by Fiore et al.

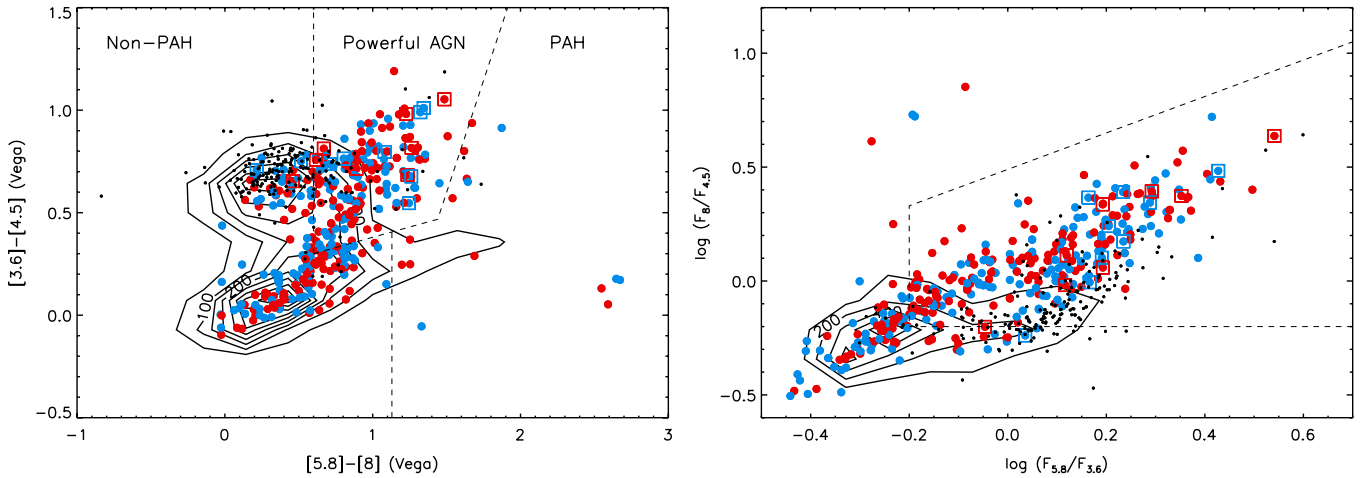


**Figure 12.** *Spitzer* IRAC colors for the X-ray sources and obscured AGN candidates in the ECDF-S. Symbols are the same as in Fig, 1. Left panel: [3.6]−[4.5] vs. [5.8]−[8] colors. *Dashed lines* show the Stern et al. (2005) AGN region and the Brand et al. (2009) threshold for PAH-dominated sources. The IR-red excess sources not detected in X-rays are mostly outside the AGN region, mainly due to their relatively blue [5.8]−[8] color. Right panel: $f_8/f_{4.5}$ vs. $f_{5.8}/f_{3.6}$ flux rations. The dashed region shows the AGN locus according to Lacy et al. (2004). As can be seen in both panels, most of the X-ray-detected 24 $\mu$m-selected sources are found in the AGN regions, suggesting that the rest-frame near-IR light is dominated by the nuclear emission. The $f_8/f_{4.5}$ flux ratio for the non-X-ray-detected sources is slightly lower than the one found in X-ray-detected sources. Together with the difference found in Figure 11 suggests that these sources are more obscured versions of the X-ray-detected AGN.

(A color version of this figure is available in the online journal.)

(2008) is deep enough to detected all their 24 $\mu$m sources. Hence, it is unlikely that these differences are due to the *K*-band flux limit either.

The main conclusion of Pope et al. (2008) is that a large majority, 80%, of their sources with $f_{24}/f_R$ >1000 (most of them also have $R - K > 4.5$) are dominated by star formation and not AGN activity. They base this conclusion in the low value of $f_8/f_{4.5}$ (their Figure 4), which is taken as evidence for a mid-IR emission dominated by a star-forming galaxy. In our sample, a large fraction of sources have $f_8/f_{4.5} < 2$ (their threshold for star formation versus AGNs), including most of the X-ray-detected 24 $\mu$m-selected sources, in which the AGNs nature derived from the X-ray luminosity and spectral shape is clear. We point out that these low $f_8/f_{4.5}$ values can easily be explained by the effects of self-absorption in the 8 $\mu$m band, as can be seen using the Nenkova et al. (2008b) torus models, and as discussed above. Pope et al. (2008) also use the X-ray spectral shape to support their conclusion of a low number of AGNs in their 24 $\mu$m-selected sample. However, as we study in more detail in Section 5.2 and was shown by Fiore et al. (2008), proper simulations are required to convert the observed X-ray spectral shape from a stacked sample that includes both AGNs and star-forming galaxies into an AGN fraction.

### *6.2. X-ray to Mid-IR Ratio and AGN Fraction*

Both X-ray and mid-IR are tracers of AGN activity, either direct emission in the former or re-radiation in the latter, and of recent star formation, although the relative X-ray emission is significantly lower in the latter. Hence, the X-ray to mid-IR ratio is particularly important in separating emission from AGN and star formation (e.g., Horst et al. 2006; Ramos Almeida et al. 2007). In Figure 13, we show the hard (observed-frame 2–8 keV) X-ray versus mid-IR (at rest-frame 12 $\mu$m) luminosity ratio as a function of rest-frame 12 $\mu$m luminosity for the X-ray sources in the ECDF-S. The rest-frame 12 $\mu$m fluxes were obtained from the quasar template spectrum of Richards et al. (2006), normalizing it to the observed MIPS 24 $\mu$m flux, which at the typical redshifts of our sources is very similar to rest-frame 12 $\mu$m. This particular wavelength was chosen since it is nearly unaffected by obscuration (e.g., Treister et al. 2009b), and it was also used by previous studies of the local AGN population (e.g., Horst et al. 2006; Gandhi et al. 2009), thus allowing for a direct comparison with our high-redshift sample. Typical values of the conversion from observed-frame 24 $\mu$m to rest-frame 12 $\mu$m are ∼0.91 − 1.26, with an average of 1.0.

The average X-ray to mid-IR ratio for the X-ray sources is 0.65, while the median is 0.4. As can be seen in Figure 13 this ratio for the X-ray-detected AGN is spread over one order of magnitude. One advantage of this ratio is that, at least for Compton-thin absorption levels, it is independent of obscuration. In fact, insignificant differences were found for the average X-ray to mid-IR ratio values for obscured and unobscured sources in the X-ray-detected sample. However, for more obscured sources, this ratio is expected to decrease, due to the effects of absorption in the hard X-ray bands. For example, for the 24 $\mu$m-selected sources individually detected in X-rays, which typically have $N_{\rm H} \simeq 10^{23}$ cm$^{-2}$, the average X-ray to mid-IR ratio is 0.43.

In order to model the effects of obscuration in the hard X-ray to mid-IR ratio for CT sources, both photoelectric absorption and Compton scattering need to be taken into account. We have done this using the template X-ray spectra of Matt et al. (1999), computed using Monte Carlo simulations. For a heavily obscured source with $N_{\rm H} > 3 \times 10^{24}$ cm$^{-2}$ the observed ratio decreases by 1–2 orders of magnitude. In the case of the IR-red excess sources, which are not individually detected in X-rays, we computed X-ray fluxes from the measured stacked signal. For each source, the average X-ray flux measured in 24 $\mu$m flux bins as described in section 5.2 was assigned. For the fainter 24 $\mu$m sources, for which no X-ray stacked signal was measured, the 1$\sigma$ background fluctuations are used as upper limits. Very similar and consistent results are obtained if the X-ray stacking is done binning sources based on 24 $\mu$m luminosity instead.

As can be seen in Figure 13, the X-ray to mid-IR ratio for the IR-red excess sources is about two orders of magnitude smaller than the average value for the X-ray-detected sample and for most sources falls in the range expected for obscuration

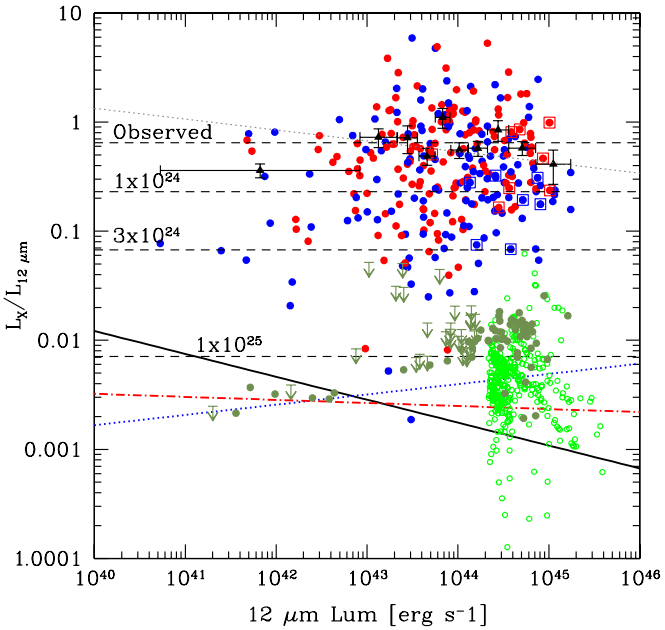


**Figure 13.** Ratio of hard X-ray to mid-IR (at rest-frame 12 $\mu$m) vs. rest-frame 12 $\mu$m luminosity. Red circles show the X-ray-detected sources with HR$> -0.3$, while the blue circles mark the sources with HR$<-0.3$. *Black triangles with error bars* show the average ratio for the X-ray-detected sources in bins of 30 sources. Circles enclosed by squares identify the X-ray-detected IR-red excess sources. The *dashed line* at a ratio of $\sim$0.6 shows the average value of $L_X/L_{12\,\mu m}$ for all the X-ray sources. The *dotted line* shows the relation between intrinsic X-ray and 12 $\mu$m luminosity for local Seyfert galaxies (Gandhi et al. 2009). *Green circles* show the location of the most luminous rest-frame 12 $\mu$m X-ray-undetected sources outside the selection region. X-ray-undetected IR-red excess sources are shown by olive circles and upper limits. X-ray luminosities were derived from the stacking signal. *Dashed* lines marked "$1 \times 10^{24}$," "$3 \times 10^{24}$," and "$1 \times 10^{25}$" show the effects of X-ray obscuration in the observed $L_X/L_{12\,\mu m}$ ratio. The thick *solid, dot-dashed and dotted lines* show the expected $L_X/L_{12\,\mu m}$ for star-forming galaxies, considering different recipes to convert star formation rates into X-ray and IR luminosities (see the text for details).

(A color version of this figure is available in the online journal.)

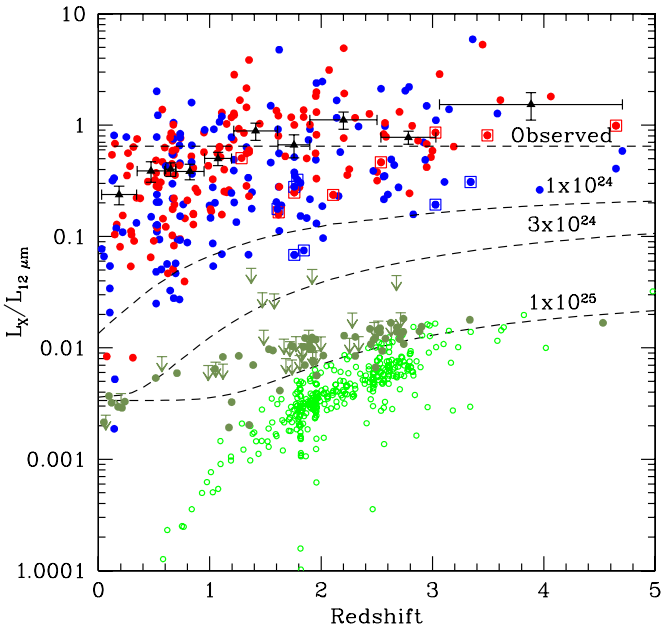


**Figure 14.** Ratio of hard X-ray to mid-IR ratio as a function of redshift. Symbols are the same as in Figure 13. The dependence of this ratio on redshift for a constant obscuration value is shown by the *dashed lines*. As can be seen here, the IR-red excess sources (*olive circles*) are mostly located in the region expected for AGN with obscurations $>5 \times 10^{24}$ cm$^{-2}$ at all redshifts and are systematically above the sample of sources with similar IR luminosities but bluer $f_{24\,\mu m}/f_R$ colors. Based on this figure we can conclude that the redshift spread of our sample does not affect our conclusions.

(A color version of this figure is available in the online journal.)

of $\sim 5 \times 10^{24}$ to $10^{25}$ cm$^{-2}$. A small fraction of the IR-red excess sample, 20%, have X-ray to mid-IR ratios lower than $7 \times 10^{-3}$. It would be very hard to explain such low ratios using obscuration, and hence it is more likely that these sources are not AGNs but star-forming galaxies. On the other hand, the observed ratio for the IR-red excess sample is significantly larger than for the sources outside our selection region, i.e., $f_{24}/f_R < 1000$ or $R - K < 4.5$, even at similar rest-frame 12 $\mu$m luminosities. The observed X-ray to mid-IR ratio for IR-red excess sources at $L_{12\,\mu m} \sim 10^{45}$ erg s$^{-1}$ is roughly 10 times larger than the values expected from the X-ray versus mid-IR luminosity for star-forming galaxies reported by Donley et al. (2008). Similar results are found if the relation between star formation rate and X-ray luminosity proposed by Gilfanov et al. (2004), which is consistent with the Ranalli et al. (2003) correlation, is used together with the relationship between IR luminosity and star formation rate of Kennicutt (1998). In order to transform rest-frame 12 $\mu$m into total IR luminosity we used the observed correlations given by Chary & Elbaz (2001) and by Takeuchi et al. (2005). The obtained rest-frame 2–10 keV luminosities are converted into observed-frame 2–8 keV assuming $\langle z \rangle = 2$ and the typical X-ray spectrum of high-mass X-ray binaries (e.g., Lutovinov et al. 2005), namely $\Gamma = 1.0$ and a high energy cutoff, $E_c$, of 20 keV. As can be seen in Figure 13, the X-ray to mid-IR ratio for the IR-red excess sources is significantly higher than the expected value for pure star-forming galaxies, thus confirming the AGN's nature for the vast majority of our sample.

To investigate a possible dependence on redshift, in Figure 14, we show the X-ray to mid-IR ratio as a function of redshift. As can be seen in this figure, the IR-red excess sources are systematically above the sample with similar IR luminosities and bluer $f_{24\,\mu m}/f_R$ colors. At the same time, the IR-red excess sources are located in the region expected for heavily obscured AGN with $N_H > 3 \times 10^{24}$ cm$^{-2}$ at all redshifts. This confirm that our conclusions are not affected by the redshift spread in our sample. It is also interesting that the fraction of star-forming galaxies in the IR-red excess sample inferred from the X-ray to mid-IR ratio is consistent with the value found from the comparison of the observed HR with the simulations of Fiore et al. (2009). While some trend is apparent, the evidence for a possible dependence of the fraction of AGN-dominated sources on mid-IR luminosity is not conclusive in our sample. Quantitatively, the fraction of star-forming galaxies (measured using a X-ray to mid-IR ratio of $7 \times 10^{-3}$ as the dividing point between AGN and star-forming galaxies) in the $10^{43} < L_{12\,\mu m}$ (erg s$^{-1}$) $< 10^{44}$ luminosity range is $4/17 = 23.5\% \pm 20\%$, considering only statistical uncertainties, while for sources with $L_{12\,\mu m} > 10^{44}$ erg s$^{-1}$ is $6/64 = 9.4\% \pm 6\%$. Furthermore, for sources with $L_{12\,\mu m} < 10^{43}$ erg s$^{-1}$ is $8/9 = 89^{+11}_{-60}\%$. The number of sources is small for lower luminosity sources ($L_{12\,\mu m} < 10^{43}$ erg s$^{-1}$), mainly due to a combination of the MIPS flux limit and our selection method. Using the same threshold in X-ray to mid-IR ratio, the fraction of star-forming galaxies for sources with $L_{12\,\mu m} > 10^{44}$ erg s$^{-1}$ and outside our obscured AGN-selection region is $80 \pm 7\%$, thus showing the clear differences in X-ray properties for our 24 $\mu$m-selected sample, even at the same mid-IR luminosities.

### 6.3. Space Density of CT AGN

Given the strong evidence presented here for the AGN's nature of the majority of the IR-red excess sources, and the very high obscuration levels that these sources show, we can use this sample to study the properties of the CT AGN population at $z \gtrsim 2$. While CT AGNs can be abundant at high redshift, $z > 2$, they only represent a small contribution to the extragalactic X-ray background, roughly 1%–2%, as was shown by Treister et al. (2009a). Because of the current uncertainties in the measurements of this background radiation and degeneracies in the assumed models, this integral constraint cannot be used to infer the number of heavily obscured sources at high redshift. While Treister et al. (2009a) discuss a possible stronger evolution for heavily obscured AGNs relative to the less-obscured sources, Della Ceca et al. (2008a) concluded that the luminosity functions of X-ray-selected CT and less-obscured AGNs were consistent with each other. These potentially contradictory results are studied in more detail here.

We measured the space density of CT AGNs using our sample of IR-red excess sources. Because of the potential incompleteness of our photometric redshift determinations we restrict our study to $z \leqslant 3$. Furthermore, taking into account the flux limit of the MIPS 24 $\mu$m data in the ECDF-S, the space density was measured only at $z < 1.1$ for sources with $L_{24\,\mu\mathrm{m}} < 10^{44}$ erg s$^{-1}$. These choices minimize the effects of incompleteness in our sample. However, other sources of incompleteness, like the *K*-band magnitude limit, required for our color selection could be also important. X-ray luminosities were estimated from the stacked X-ray signal, as described in Section 6.2.

In Figure 15, we present our measurements of the space density as a function of luminosity (triangles) together with the expectations from three different $z = 0$ CT AGN luminosity functions: Della Ceca et al. (2008a), Treister et al. (2009a) and Yencho et al. (2009). For the latter, the X-ray luminosity function for all AGNs was converted into a CT AGN luminosity function assuming the luminosity dependence of the obscured AGN fraction given by Treister et al. (2009a), normalized to match the INTEGRAL measurements at low luminosities. Except for the lack of a decline at low luminosities in the work of Della Ceca et al. (2008a), the three curves are consistent with each other. In order to compare with these $z = 0$ expectations, the ECDF-S measurements, together with other values obtained from the literature were "de-evolved" using the corresponding evolution form for each luminosity function. The differences between observations and expectations must be due to the assumed evolution in the latter. While in all these works a luminosity-dependent density evolution was assumed, different parameter values were obtained in each case. For example, Della Ceca et al. (2008a) assumed a strong evolution for all AGNs, while Treister et al. (2009a) used the values estimated by Ueda et al. (2003), which give a much shallower evolution. As can be seen in this figure, while both the Della Ceca et al. (2008a) and Yencho et al. (2009) provide an acceptable description of the observational data, the values obtained using the Ueda et al. (2003) evolution fall systematically above the $z = 0$ curve. Hence, these results indicate that a similar shape of the luminosity function is found for CT AGN and less-obscured sources, in agreement with the conclusions of Della Ceca et al. (2008a).

In order to study in more detail the evolution of the CT AGN space density, in Figure 16, we present our measurements of the CT AGN space density as a function of redshift. A reasonable

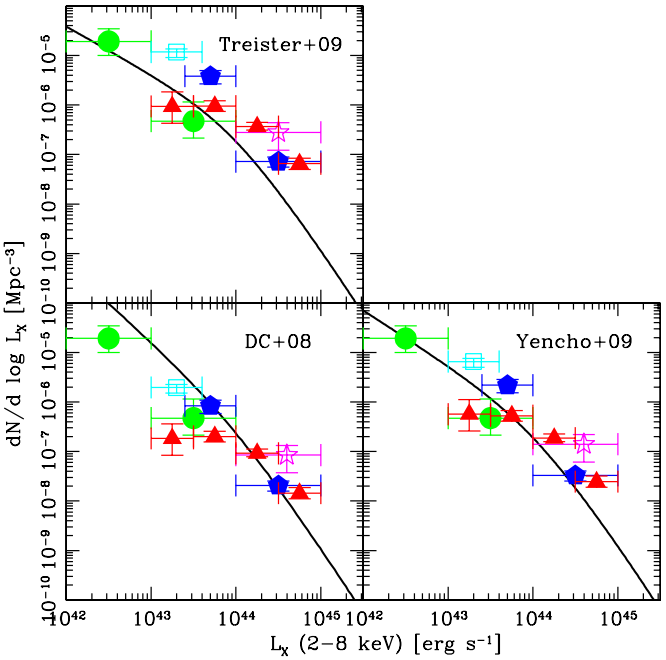


**Figure 15.** Three estimates (thick lines) of the hard X-ray luminosity function of Compton thick AGN at $z = 0$, as measured by Treister et al. (2009a) (upper left panel), Della Ceca et al. (2008a; lower left panel), and Yencho et al. (2009; right panel). Symbols with error bars show the measurements of the space density of Compton thick AGN as a function of hard X-ray luminosity, de-evolved to $z = 0$ following the corresponding evolution for each work (see text for details). Filled triangles: this paper, filled circles: Treister et al. (2009a), filled pentagons: Fiore et al. (2009), open square: Daddi et al. (2007), star: Alexander et al. (2008).

(A color version of this figure is available in the online journal.)

agreement, in particular at $z < 1$, is found between both our observed values and others obtained from the literature and the luminosity function and evolution assumed by Yencho et al. (2009). However, at higher redshifts and higher luminosities clear discrepancies are found. This was already pointed out by Treister et al. (2009a), who concluded that this difference of a factor of 2–3 could most likely be due to either incompleteness in the *Swift*/BAT and INTEGRAL CT AGN samples at $z = 0$ used to fix the luminosity function normalization (because reflection-dominated AGNs are missed) or to contamination by other types of sources in the observed values at high redshifts. However, after adding the measurements obtained using the IR-red excess sources in the ECDF-S it appears not only that the systematic difference is still present but perhaps more importantly that there is a strong increase in the number of CT AGNs from $z \simeq 1.7$ to 2.4.

As can be seen in Figure 13, most of the sources with only upper limits to their X-ray to mid-IR emission ratios have mid-IR luminosities lower than $10^{44}$ erg s$^{-1}$. Hence, excluding these sources from our measurements of the space density of CT AGNs as a function of redshift presented in Figure 16 does not change these values significantly. For sources with $L_X > 10^{43}$ erg s$^{-1}$ if those with only upper limits are excluded the space density is reduced by ∼30%. In Figure 15, where we presented the space density of CT sources as a function of hard X-ray luminosity, the effects of excluding sources with upper limits are more relevant for the less-luminous sources. In the $43 < \log(L_X[\mathrm{erg\ s^{-1}}]) < 43.5$, the space density is reduced by ∼70% if upper limit sources are excluded. Similarly, in the $43.5 < \log(L_X[\mathrm{erg\ s^{-1}}]) < 44$, the space density should be reduced by ∼60% by excluding the upper limits from the sample, while

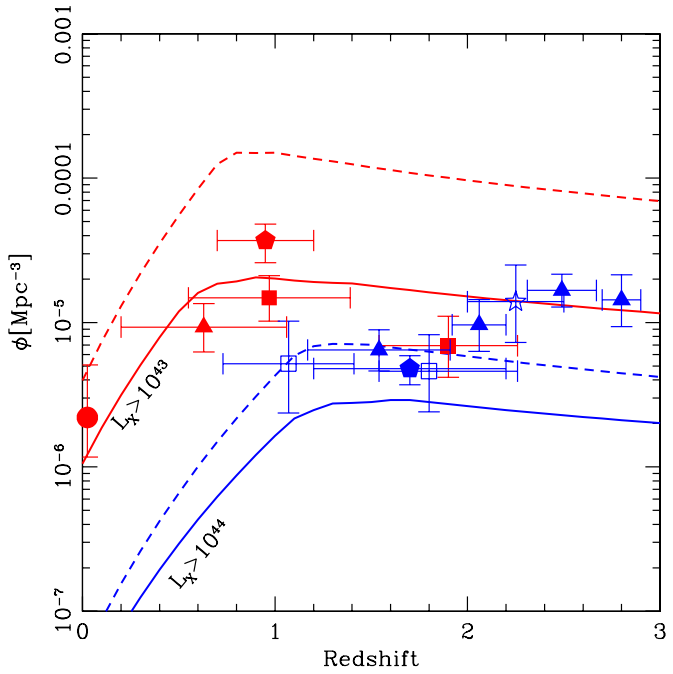


**Figure 16.** Space density of Compton thick AGN as a function of redshift. Filled triangles show the measurements described in this paper. Squares: space density from the work of Tozzi et al. (2006). Star: measurement by Alexander et al. (2008). Pentagons: values reported by Fiore et al. (2009). Solid lines show the expected space density of Compton thick AGN from the luminosity function of Yencho et al. (2009), with the overall normalization fixed to the results of Treister et al. (2009a), while the dashed lines show the expectations based on the luminosity function of Della Ceca et al. (2008a). Red symbols show measurements and expectations for $L_X > 10^{43}$ erg s$^{-1}$ sources, while the blue symbols are for $L_X > 10^{44}$ erg s$^{-1}$. While for the lower luminosity sources a good agreement is found between observations and expectations, higher luminosity sources lie well above the luminosity function. Furthermore, the new measurements seem to indicate as strong increase in the number of high-luminosity heavily obscured sources at $z > 2$.

(A color version of this figure is available in the online journal.)

at higher luminosities the effect is less than 10% and hence negligible.

The strong evolution in the number of CT AGNs at high redshift presented in Figure 16 was not indicated by any existing luminosity function. It is unlikely that this evolution is due to selection effects, as results from different fully independent surveys and selection techniques are combined in Figure 16, namely X-ray-selected sources from Tozzi et al. (2006), 24 $\mu$m-selected sources from Fiore et al. (2009) and our work, and the sample of CT AGN found using mid-IR spectroscopy by Alexander et al. (2008). If confirmed, this result indicates a very large number of heavily obscured AGN at $z \simeq 2.5$ followed by a strong decline, by a factor of $\sim$3, at $z = 1.5$. This result can be interpreted in the context of the galaxy evolution models of Hopkins et al. (2008), where quasar activity is driven by galaxy mergers and the supermassive black hole is initially completely surrounded by dust, before radiation pressure removes it and a "classical" unobscured quasar is visible. The consequences of this observed rapid evolution are beyond the scope of this work and will be studied in further detail in an upcoming paper.

## 7. CONCLUSIONS

We presented a study of heavily obscured (CT) AGN candidates selected from their optical, near and mid-IR colors. These sources were selected by requiring $f_{24\,\mu\mathrm{m}}/f_R > 1000$ and $R - K > 4.5$. Using this selection method, we found a total of 211 infrared-red excess sources in the ECDF-S. Of these, 18 were individually detected in the Chandra 250 ks observations of this field. These sources are moderately obscured, with $N_{\mathrm{H}} = 10^{22}$–$10^{23}$ cm$^{-2}$, according to their X-ray spectra. Two of these sources have $N_{\mathrm{H}} > 10^{-24}$ cm$^{-2}$, and therefore are classified as CT AGNs, including one at $z = 4.65$. The average redshift for the X-ray-detected sample is $\langle z \rangle \sim 2.37$ (median = 1.85), in agreement with previous studies. By performing spectral fitting to the observed optical to near-IR fluxes of the X-ray-detected sources we found that the host galaxies have typical stellar masses of $10^{11.7} M_{\odot}$ and are subject to moderate extinction, with $\langle E(B-V) \rangle = 0.6$.

For the X-ray-undetected sources, we found a slightly lower average redshift of $\langle z \rangle \sim 1.9$, based on photometric measurements only. We found that in general the X-ray-detected sources are brighter in both the 24 $\mu$m and optical bands compared to the undetected ones. Taking advantage of the low Chandra background, we performed X-ray stacking, finding a significant ($\gtrsim 3\sigma$) detection in both the soft and hard bands. The average X-ray flux of these sources is $\sim 8 \times 10^{-17}$ erg cm$^{-2}$ s$^{-1}$, indicating that in order to detect these sources individually, exposure times of $\sim$10 Ms with Chandra would be required. Taken at face value, the observed average HR of 0.13 corresponds to a $N_{\mathrm{H}}$ of $\sim 2 \times 10^{23}$ cm$^{-2}$. However, this can also be interpreted as the effects of combining a population of 90% CT AGNs and 10% star-forming galaxies, which in general have softer X-ray spectra. From this analysis we found marginal evidence for a small dependence of the fraction of AGNs relative to star-forming galaxies on 24 $\mu$m flux, going from $\sim$95% for the brightest sources to $\sim$80% at the lowest flux bin. The spectral fitting analysis performed to these sources indicate that in general there is evidence for substantial young stellar populations, younger than 100 Myr. This suggests that these sources are simultaneously experimenting significant star formation and heavily obscured AGNs activity. We did not found significant differences in the stellar masses and extinction values for the host galaxies of the X-ray-detected and undetected IR-red excess sources.

The X-ray-undetected IR-red excess sources have redder $f_{24}/f_8$ flux ratios than those detected in X-rays. The average $f_{24}/f_8 \simeq 25$ is hard to explain assuming the observed spectra of ultra-luminous infrared galaxies, however it can be well explained by dust re-radiation models in which the effects of self-absorption are important. Similarly, while the IRAC colors of most of these sources are outside the typical AGN region, this can be explained by the effects of absorption and/or a dominance of the near-IR emission by the host galaxy. In contrast, the X-ray-detected sources have IRAC colors consistent with those of less-obscured AGN. The X-ray-to-mid-IR ratio for the X-ray-detected sources is similar to the average value for the overall X-ray population. For the X-ray-undetected sources this ratio is $\sim$2 orders of magnitude lower than for the sample individually detected in X-rays. This ratio is consistent with obscuration levels of $\sim 5 \times 10^{24}$ to $10^{25}$ cm$^{-2}$, while it is significantly larger than the relative X-ray emission expected from star formation activity alone. Using a constant threshold in X-ray to mid-IR flux ratio, we found that the fraction of AGN in our sample should be $\sim$80%, consistent with the value found from the analysis of the stacked X-ray signal. We also found a similar dependence of the AGN fraction on 24 $\mu$m luminosity ranging from $\sim$90% at the bright end to only $\sim$10% for the faintest sources.

Finally, we studied the space density of sources implied by our sample of 24 $\mu$m-selected heavily obscured AGN candidates. While at lower redshifts and luminosities we found a good agreement with population synthesis models and extrapolations of existing X-ray luminosity functions to higher obscuration, we found significant excesses for high-luminosity sources at high redshifts. Furthermore, we found a strong evolution in the number of sources with $L_X > 10^{44}$ erg s$^{-1}$ from $z = 1.5$ to 2.5. This can be interpreted as evidence for a relatively short-lived heavily obscured phase before the strong radiation pressure removes the surrounding dust and turns the sources into an unobscured quasar.

We thank Moshe Elitzur, Maia Nenokva and Robert Nikutta for providing us their CLUMPY models in electronic format, and Takamitsu Miyaji for his support of the CSTACK tool. We are grateful for the help of Youichi Ohyama reducing the MOIRCS data and for useful discussions with Dave Sanders, Priya Natarajan, David Rupke, Len Cowie and Amy Barger. We thank the anonymous referee for very helpful comments. Support for the work of E.T. was provided by the National Aeronautics and Space Administration through Chandra Postdoctoral Fellowship Award Number PF8-90055 issued by the *Chandra* X-ray Observatory Center, which is operated by the Smithsonian Astrophysical Observatory for and on behalf of the National Aeronautics Space Administration under contract NAS8-03060. E.G. acknowledges support from NSF grant AST-0807570. This research has made use of NASA's Astrophysics Data System.

*Facilities:* VLT:Melipal (VIMOS), VLT:Yepun (SINFONI), CXO (ACIS), *Spitzer* (IRAC, MIPS), Max (WFI), Blanco (MOSAIC-II, ISPI), Subaru (suprimecam)

## REFERENCES

Alexander, D. M., et al. 2003, AJ, 126, 539
Alexander, D. M., et al. 2008, ApJ, 687, 835
Armus, L., et al. 2007, ApJ, 656, 148
Barger, A. J., Cowie, L. L., Bautz, M. W., Brandt, W. N., Garmire, G. P., Hornschemeier, A. E., Ivison, R. J., & Owen, F. N. 2001, AJ, 122, 2177
Barger, A. J., Cowie, L. L., Mushotzky, R. F., Yang, Y., Wang, W.-H., Steffen, A. T., & Capak, P. 2005, AJ, 129, 578
Barmby, P., et al. 2006, ApJ, 642, 126
Benítez, N. 2000, ApJ, 536, 571
Bolzonella, M., Miralles, J.-M., & Pelló, R. 2000, A&A, 363, 476
Bonnet, H., et al. 2004, Messenger, 117, 17
Brammer, G. B., van Dokkum, P. G., & Coppi, P. 2008, ApJ, 686, 1503
Brand, K., et al. 2006, ApJ, 644, 143
Brand, K., et al. 2009, ApJ, 693, 340
Brandt, W. N., & Hasinger, G. 2005, ARA&A, 43, 827
Brandt, W. N., Hornschemeier, A. E., Schneider, D. P., Alexander, D. M., Bauer, F. E., Garmire, G. P., & Vignali, C. 2001, ApJ, 558, L5
Calzetti, D., Armus, L., Bohlin, R. C., Kinney, A. L., Koornneef, J., & Storchi-Bergmann, T. 2000, ApJ, 533, 682
Cardamone, C. N., et al. 2008, ApJ, 680, 130
Chary, R., & Elbaz, D. 2001, ApJ, 556, 562
Cowie, L. L., Garmire, G. P., Bautz, M. W., Barger, A. J., Brandt, W. N., & Hornschemeier, A. E. 2002, ApJ, 566, L5
Croton, D. J., et al. 2006, MNRAS, 365, 11
Daddi, E., et al. 2007, ApJ, 670, 173
Della Ceca, R., et al. 2008a, A&A, 487, 119
Della Ceca, R., et al. 2008b, Mem. Soc. Astron, Ital., 79, 65
Dey, A., et al. 2008, ApJ, 677, 943
Donley, J. L., Rieke, G. H., Pérez-González, P. G., & Barro, G. 2008, ApJ, 687, 111
Eisenhauer, F., et al. 2003, Proc. SPIE, 4841, 1548
Fabbiano, G. 1989, ARA&A, 27, 87
Fazio, G. G., et al. 2004, ApJS, 154, 10
Ferrarese, L., Pogge, R. W., Peterson, B. M., Merritt, D., Wandel, A., & Joseph, C. L. 2001, ApJ, 555, L79
Ferreras, I., & Silk, J. 2002, MNRAS, 336, 1181
Fiore, F., et al. 2008, ApJ, 672, 94
Fiore, F., et al. 2009, ApJ, 693, 447
Fruscione, A., et al. 2006, Proc. SPIE, 6270, 60
Gandhi, P., Horst, H., Smette, A., Hönig, S., Comastri, A., Gilli, R., Vignali, C., & Duschl, W. 2009, A&A, 502, 457
Gawiser, E., et al. 2006a, ApJS, 162, 1
Gawiser, E., et al. 2006b, ApJ, 642, L13
Gebhardt, K., et al. 2000, ApJ, 539, L13
Georgantopoulos, I., Georgakakis, A., Rowan-Robinson, M., & Rovilos, E. 2008, A&A, 484, 671
Gilfanov, M., Grimm, H.-J., & Sunyaev, R. 2004, MNRAS, 347, L57
Gilli, R., Comastri, A., Brunetti, G., & Setti, G. 1999, New Astron. J., 4, 45
Gilli, R., Comastri, A., & Hasinger, G. 2007, A&A, 463, 79
Grazian, A., et al. 2006, A&A, 449, 951
Hayashino, T., et al. 2000, Proc. SPIE, 4008, 397
Hildebrandt, H., et al. 2006, A&A, 452, 1121
Hopkins, P. F., Hernquist, L., Cox, T. J., Di Matteo, T., Robertson, B., & Springel, V. 2006, ApJS, 163, 1
Hopkins, P. F., Hernquist, L., Cox, T. J., & Kereš, D. 2008, ApJS, 175, 356
Horst, H., Smette, A., Gandhi, P., & Duschl, W. J. 2006, A&A, 457, L17
Ichikawa, T., et al. 2006, Proc. SPIE, 6269, 38
Kalberla, P. M. W., Burton, W. B., Hartmann, D., Arnal, E. M., Bajaja, E., Morras, R., & Pöppel, W. G. L. 2005, A&A, 440, 775
Kaviraj, S., et al. 2007, ApJS, 173, 619
Kennicutt, R. C., Jr. 1998, ApJ, 498, 541
Kewley, L. J., Groves, B., Kauffmann, G., & Heckman, T. 2006, MNRAS, 372, 961
Lacy, M., et al. 2004, ApJS, 154, 166
Lehmer, B. D., et al. 2005, ApJS, 161, 21
Luo, B., et al. 2008, ApJS, 179, 19
Lutovinov, A., Revnivtsev, M., Gilfanov, M., Shtykovskiy, P., Molkov, S., & Sunyaev, R. 2005, A&A, 444, 821
Magorrian, J., et al. 1998, AJ, 115, 2285
Maraston, C. 2005, MNRAS, 362, 799
Matt, G., Pompilio, F., & La Franca, F. 1999, New Astron. J., 4, 191
Menci, N., Fontana, A., Giallongo, E., Grazian, A., & Salimbeni, S. 2006, ApJ, 647, 753
Mignano, A., et al. 2007, A&A, 462, 553
Murphy, E. J., Chary, R.-R., Alexander, D. M., Dickinson, M., Magnelli, B., Morrison, G., Pope, A., & Teplitz, H. I. 2009, ApJ, 698, 1380
Nandra, K., George, I. M., Mushotzky, R. F., Turner, T. J., & Yaqoob, T. 1997, ApJ, 476, 70
Nenkova, M., Ivezić, Ž., & Elitzur, M. 2002, ApJ, 570, L9
Nenkova, M., Sirocky, M. M., Ivezić, Ž., & Elitzur, M. 2008a, ApJ, 685, 147
Nenkova, M., Sirocky, M. M., Nikutta, R., Ivezić, Ž., & Elitzur, M. 2008b, ApJ, 685, 160
Pope, A., et al. 2008, ApJ, 689, 127
Ramos Almeida, C., Pérez García, A. M., Acosta-Pulido, J. A., & Rodríguez Espinosa, J. M. 2007, AJ, 134, 2006
Ranalli, P., Comastri, A., & Setti, G. 2003, A&A, 399, 39
Richards, G. T., et al. 2006, ApJS, 166, 470
Rieke, G. H., et al. 2004, ApJS, 154, 25
Rix, H.-W., et al. 2004, ApJS, 152, 163
Rousselot, P., Lidman, C., Cuby, J.-G., Moreels, G., & Monnet, G. 2000, A&A, 354, 1134
Salvato, M., et al. 2009, ApJ, 690, 1250
Sanders, D. B., Soifer, B. T., Elias, J. H., Madore, B. F., Matthews, K., Neugebauer, G., & Scoville, N. Z. 1988, ApJ, 325, 74
Schawinski, K., Thomas, D., Sarzi, M., Maraston, C., Kaviraj, S., Joo, S.-J., Yi, S. K., & Silk, J. 2007, MNRAS, 382, 1415
Schawinski, K., Virani, S., Simmons, B., Urry, C. M., Treister, E., Kaviraj, S., & Kushkuley, B. 2009, ApJ, 692, L19
Schawinski, K., et al. 2006, Nature, 442, 888
Spergel, D. N., et al. 2007, ApJS, 170, 377
Steffen, A. T., Barger, A. J., Cowie, L. L., Mushotzky, R. F., & Yang, Y. 2003, ApJ, 596, L23
Stern, D., et al. 2005, ApJ, 631, 163
Suzuki, R., et al. 2008, PASJ, 60, 1347
Szokoly, G. P., et al. 2004, ApJS, 155, 271
Takeuchi, T. T., Buat, V., Iglesias-Páramo, J., Boselli, A., & Burgarella, D. 2005, A&A, 432, 423
Taniguchi, Y. 2004, in Proc. of Japan-German Seminar, Studies of Galaxies in the Young Universe with New Generation Telescope, ed. N. Arimoto & W. J. Duschl, 107
Taylor, E. N., et al. 2009, ApJS, 183, 295
Tozzi, P., et al. 2006, A&A, 451, 457

Treister, E., Gawiser, E., van Dokkum, P., Lira, P., Urry, M., & The Musyc Collaboration., 2007, Messenger, 129, 45
Treister, E., & Urry, C. M. 2005, ApJ, 630, 115
Treister, E., Urry, C. M., & Virani, S. 2009a, ApJ, 696, 110
Treister, E., et al. 2004, ApJ, 616, 123
Treister, E., et al. 2005, ApJ, 621, 104
Treister, E., et al. 2006, ApJ, 640, 603
Treister, E., et al. 2009b, ApJ, 693, 1713
Ueda, Y., Akiyama, M., Ohta, K., & Miyaji, T. 2003, ApJ, 598, 886
Virani, S. N., Treister, E., Urry, C. M., & Gawiser, E. 2006, AJ, 131, 2373
Wolf, C., et al. 2004, A&A, 421, 913
Yencho, B., Barger, A. J., Trouille, L., & Winter, L. M. 2009, ApJ, 698, 380